Data Analysis Techniques in Gravitational Wave Astronomy

A thesis submitted towards partial fulfilment of
BS-MS Dual Degree Programme

by

SWETHA BHAGWAT

Indian Institute of Science Education and Research,
IISER, Pune

under the guidance of

Prof. Sanjit Mitra and Prof. Sanjeev Dhurandhar

Inter-University Centre for Astronomy and
Astrophysics, IUCAA, Pune

Co-supervisor : Prof. Tarun Souradeep, IUCAA, Pune

Local Coordinator : Prof. Ramana Athreya , IISER-Pune

April 2013

Certificate

This is to certify that this thesis entitled Data Analysis Techniques in Gravitational Wave Astronomy submitted towards the partial fulfilment of the BS-MS dual degree programme at the Indian Institute of Science Education and Research Pune represents original research carried out by SWETHA BHAGWAT at Inter-University Centre for Astronomy and Astrophysics, IUCAA, under the supervision of Prof. SANJIT MITRA during the academic year 2012-2013.

Student
SWETHA
BHAGWAT

Supervisor
Dr. SANJIT
MITRA

Acknowledgements

It has been a great experience working on this project and I would like to share credits with many around me for helping me through it. First of all, I would like to express my deepest gratitude to Prof. Sanjeev Dhurandhar for introducing me to gravitational wave astronomy and for constantly guiding me for nearly three years now. Without his invaluable guidance and effort, this work would not have been possible. I also want to truly thank Prof. Sanjit Mitra for being an such encouraging, enthusiastic and friendly supervisor. Not only did I learn a lot while working with him, but I also thoroughly enjoyed it. I am also indebted to Jayanti for helping me throughout the course of this project - thanks for the long discussions on the project, the valuable advice on proper documentation and of course, for the interesting tea-time conversations. Also, I want to thank Gaurav for giving me helpful comments every now and then. Further, I would like to acknowledge all the members of CMBR group, especially Prof. Tarun Sauradeep for being very supportive throughout the duration of my project. I would also wish to thank our collaborators- Andy and Tito from AEI, Hannover for those insightful discussions, which has gone into building the first part of this thesis.

Next, I want to sincerely thank my parents and my brother, Ganesh for their ever-encouraging nature. I really admire their desire to understand my work and their patience to listen to me, each time I try to explain it to them. Their encouragement has been crucial to me.

This acknowledgement would be severely incomplete without thanking my friends. Thanks a lot, Ankita, Roshni, Sruti, Pooja, Lokesh, Borg, Sid and AC for all the fun moments that we have shared. I specially want to thank Krishna, Amruta and Aparna for being with me all the time and most of all for being such awesome friends. Without the wonderful and lively company of these people, it would be a very boring and dry experience. I am also indebted to Sachit and Archisman for helping me at different stages and for the long conversations on various interesting problems. At this point, I think it is also fair to thank the many many bands like Pink Floyd and Dire Straits whose music has kept me entertained while running my time-consuming and patience-testing MATLAB codes.

Finally, I would like to thank IISER for giving me a platform to explore and work on research project from my very first year of under-graduation. I

would like to end with a very special thanks to Prof. Ramana Athreya for agreeing to be my mentor and being supportive and encouraging all along in his own unique way.

Abstract

As the field of gravitational wave astronomy strides rapidly towards its first direct detection, developing efficient data analysis strategies become crucial due to the low signal to noise ratio in the data. The noise level is comparable to the signal strength and this poses a serious threat of false detection. The first part of my thesis addresses the issues of false-alarm caused by an important family of glitches that can be modeled as sine-Gaussian in the data analysis technique used for detecting signals from coalescing compact binaries. We develop three approximate analytical expressions that allows us to predict the nature of spurious triggers generated by these glitches. The second part of my thesis concerns with the map-making in stochastic gravitational wave background. Here again, the weakness of the signal and the nature of the detector beam makes the problem non-trivial. We incorporate a prior knowledge on the source distribution through regularization functions and investigate the improvement in quality of reconstructed map. This work will have implications in placing an upper limit on the source parameter in the absence of detection.

Contents

1 An Overview : Gravitational Waves **5**

1.1 Introduction and Motivation 5

1.2 Formalism 6

1.3 Interferometric Gravitational Wave Detectors 7

1.4 Sources of Gravitational Waves 9

2 Compact Binary Coalescence **11**

2.1 Gravitational Waves Emitted During Compact Binary Coalescence 12

2.2 The Technique of Matched Filtering 14

2.3 An Introduction to Searches for Binary Coalescence 16

3 Effect of sine-Gaussian Glitches on Searches for Binary Coalescence **17**

3.1 Sine-Gaussian Glitches 18

3.2 Chirp Waveform 19

3.3 Effect of sine-Gaussian Glitches on Matched Filtering 21

3.3.1 Correlation 21

3.3.2 Numerical Implementation 22
3.3.3 Approximation 1 23
3.3.4 Approximation 2 26
3.3.5 Approximation 3 28
3.4 Conclusion 29

4 Stochastic Gravitational Wave Background 31

4.1 Radiometry 31
4.2 The Beam and SGWB map-making 32
4.3 Statistical Properties of Signal and Noise 34

5 Probing Anisotropy of Stochastic gravitational wave background using prior knowledge on source distribution 36

5.1 Bayesian Analysis 38
5.1.1 Most Likely Solution S_{ml} 38
5.1.2 Ill-Posed Problem and Regularization 38
5.1.3 Most Probable Solution S_{mp} 40
5.1.4 Strength of Regularization 41
5.2 Quantifying the Quality of Reconstruction - Normalised Scalar Product (NSP) 43
5.3 Numerical Implementation of Regularized Deconvolution . . . 43
5.3.1 Pixelization Scheme 44
5.3.2 Simulating Source Map 44
5.3.3 Quadratic Regularization function 44

5.3.4 Computing S_{ml} and S_{mp} 45

5.3.5 Calculating the Hessian Matrix C 46

5.4 Results of Source Reconstruction using Gradient Regularization 47

5.5 Source Reconstruction Using Prior Knowledge on Source Location 48

5.6 Bias Introduced by Regularization 51

5.7 Discussion 53

References **58**

A Stationary Phase Approximation **62**

B Derivation of expression for S_{ml} **63**

C Derivation of expression for S_{mp} **64**

Chapter 1

An Overview : Gravitational Waves

1.1 Introduction and Motivation

Einstein's theory of relativity tells us that a changing matter-energy distribution leads to a changing space-time curvature. Far away from the source where the gravitational field is weak, one can approximate the gravitational effects of changing mass-energy distribution as perturbations on otherwise flat Minkowski space-time. These perturbations of the space-time metric propagate as gravitational waves (GW) at the speed of light. Any varying mass quadrupole generates gravitational waves.

The experimental verification of Einstein's theory of gravity has been limited to a few astrophysical phenomenons like perihelion precession of Mercury, bending of light and gravitational redshift. Although these phenomenons strongly indicate the correctness of the theory, they are not sufficient proofs. The direct detection of gravitational waves, on the other hand, would serve as a concrete test of Einstein's theory of relativity. In the light of current quest for unified theory, it has to be emphasized that validating the theory of gravitation is crucial and has a great bearing to the development of fundamental physics. Studying the properties of the gravitational waves will either substantiate or revolutionize our current theoretical understanding of gravity. Discussions on this can be found in work like [Vallisneri, 2012, Arun and Pai, 2013, Chamberlin and Siemens, 2012].

Further, a confluence of GW astronomy with EM astronomy would offer us a great advantage to understand many astrophysical phenomenons. Gravitational radiations contain information that is hidden to electromagnetic astronomy. For instance, using EM radiation one can only get an indirect inference on the dynamics of black holes. On the contrary, detecting the waveform of gravitational waves emitted by the mergers of black hole binaries would be a direct detection of these objects. It can give us crucial information about the masses and spins of the black holes. Studying gravitational wave emission will also help us develop an insight to the dynamics in strong gravitational field regime.

Although there has been no direct detection till today, there is a strong but indirect evidence, confirming the existence of gravitational waves. The Nobel Prize winning work of Russell Hulse and Joseph Taylor shows that the observed orbital period of the binary system PSR $1913 + 16$ (better known as Hulse-Taylor binary pulsar), decreases exactly (with an error less than 0.2 %) as predicted by the theory of relativity ([Weisberg and Taylor, 2004]). As they orbit, energy is lost as gravitational radiation. The binary pulsar system will inspiral and eventually merge.

There have been extensive efforts towards direct detection of GW in the past few decades using Weber bars, spherical gravitational-wave antennas, pulsar timing arrays and laser interferometric detectors. Since the gravitational coupling constant is very small ($G = 6.7\times10^{-11}Nm^2kg^{-2}$), the interaction of GW with the detector is extremely weak. As a consequence, the GW signals are so faint that their strength is comparable to the intrinsic noise produced in the detector. Typically, the order of magnitude of the strain amplitude generated in a kilometer scale interferometer is about 10^{-22}. This makes their direct detection one of the most challenging problems . A detailed review can be found on this subject can be found in ([Thorne, 1997, Hough et al., 2005]).

1.2 Formalism

Gravitational waves are solutions to the Einstein's equation in the weak field limit. In a region where gravitational field is weak, the space-time metric can be approximated as,

$$g_{\alpha\beta} = \eta_{\alpha\beta} + h_{\alpha\beta} \tag{1.1}$$

Where $h_{\alpha\beta}$ is small perturbation on the flat space-time $\eta_{\alpha\beta}$. Perturbation are such that $|h_{\alpha\beta}| \ll 1$. Trace-reversed metric perturbation is defined as,

$$\bar{h}_{\alpha\beta} := h_{\alpha\beta} - \frac{1}{2}\eta_{\alpha\beta}h \tag{1.2}$$

Where,

$$h := \eta_{\alpha\beta}h^{\alpha\beta} \tag{1.3}$$

One can exploit the gauge freedom to demand that the spatial metric perturbations should have only transverse components. Mathematically,

$$\bar{h}^{\alpha\beta}_{,\beta} = 0 \tag{1.4}$$

Further, trace of the metric perturbation is also set to zero.

$$\bar{h}^{\alpha}_{\alpha} = 0 \tag{1.5}$$

Such a gauge is referred to as transverse-traceless (TT) gauge.

Since the perturbations are small, the contribution from higher order term in $h_{\alpha\beta}$ can be neglected. The Linearized Einstein's equation in TT gauge simplify to a tensor wave equation and solutions to it are gravitational waves.

$$\Box\bar{h}_{\alpha\beta} = 0 \tag{1.6}$$

$$\bar{h}_{\alpha\beta} = A\mathbf{e}_{\alpha\beta}\mathbf{e}^{\mathbf{ik}_\gamma\mathbf{x}^\gamma} \tag{1.7}$$

$\mathbf{e}_{\alpha\beta}$ denote the polarization tensor. In the TT gauge, one can show that only 2 of the 16 components $h_{\alpha\beta}$ turn out to be independent. These correspond to the two polarization of the gravitational wave - the plus polarization h_+ and the cross polarization $h_\times$.

1.3 Interferometric Gravitational Wave Detectors

As gravitational waves pass, they stretch and squeeze the space transverse to the direction of their propagation. The laser interferometric detectors use this effect to detect a passing gravitational wave. They are essentially sophisticated Michaelson interferometer with kilometer long arms that are nearly orthogonal to each other. In the interferometer, a beam splitter splits and sends the incident high power laser beam to the two orthogonal arms. A

highly polished mirror is placed at the end of each arm to reflect these laser beams back to the beam splitter. The interference of these beams are then studied to infer the differential change in its arm-length. A simplified setup of the detector is shown in Figure 1.1.

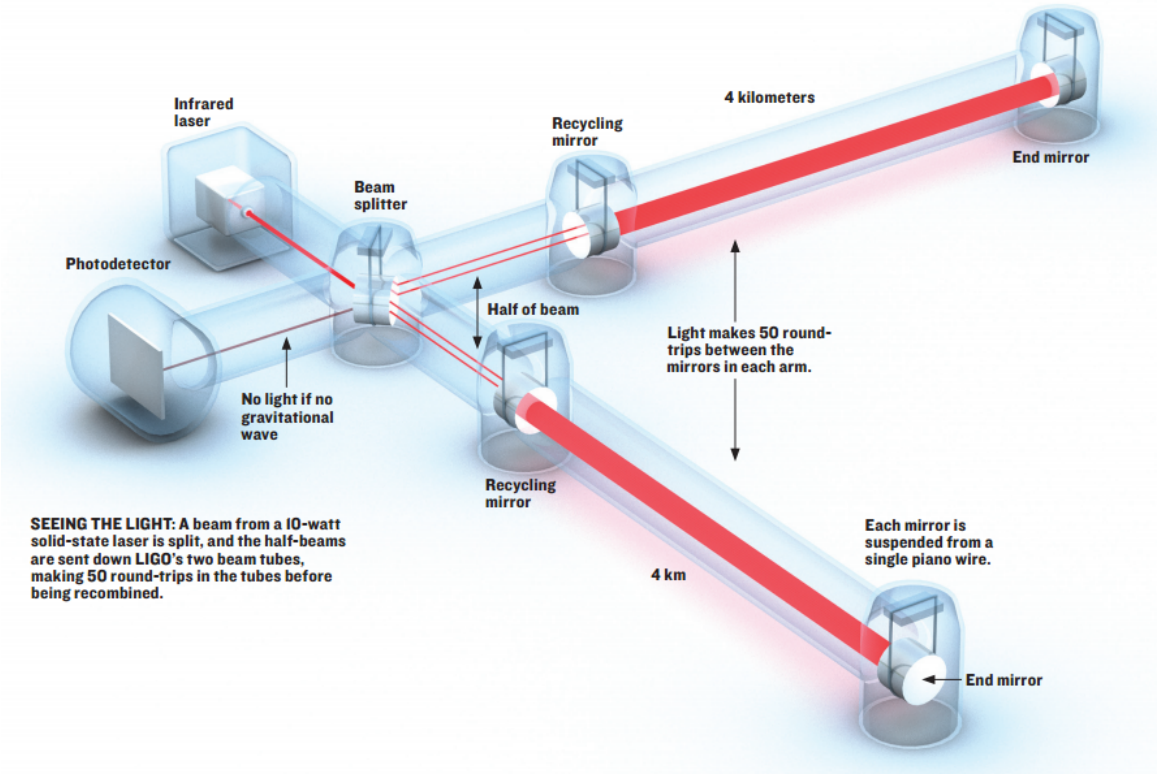

(a)

Figure 1.1: This schematic diagram of laser interferometric gravitational-wave detector is taken from *Page*44 of IEEE Spectrum | July 2006 | NA.

The mirrors of the interferometer can be considered to be free falling test masses. The free falling mirrors follow a geodesic equation. In the proper frame of the detector, mirrors move as the space-time fabric is stretched and squeezed. A differential change in the arm length ΔL, leads to a change in the light travel path. The phase shift $\Delta\Phi$ of the light emerging from the two arms is given by,

$$\Delta\Phi = n\frac{\Delta L}{\lambda} \tag{1.8}$$

Here, n is the number times the light bounces back and forth in the arm and λ is the wavelength of the gravitational wave. The design of the interferometer

is such that in the absence of gravitation wave, the interference leads to a dark fringe. The phase shift caused by a passing gravitational wave creates an interference pattern.

The differential length change between the mirrors in the detector creates a strain. This strain ($\frac{\Delta L}{L}$) is measured as a signal.

$$\frac{\Delta L}{L} = h(t) \tag{1.9}$$

The stretching and squeezing of the space-time happens as a superposition of effects due to the plus and the cross polarizations of the passing gravitational wave. The strain developed due to the motion of the mirrors can thus be expressed as a linear combination of the h_+ and $h_\times$ polarization.

$$h(t) = F_+ h_+(t) + F_\times h_\times(t) \tag{1.10}$$

F_+ and $F_\times$ are coefficients that capture the information of orientation of the detector with respect to the source.

A network of highly sensitive ground based laser interferometers established around the globe are working towards the first direct detection of gravitational wave signal. The largest of them are the two LIGO detectors with a 4 km arm length located in Livingston, Louisiana and Hanford, Washington. VIRGO and GEO are gravitational wave observatories located in Europe. The frequency bandwidth of these detectors are limited by their intrinsic noise. At low frequencies seismic noise, thermal noise from the suspension and radiation pressure noise cause a serious hindrance. At high frequency (above 200 Hz) photon shot noise is a dominant noise source ([Abbott et al., 2009]). Advanced LIGO detectors are designed to have to a broadband of frequency around 100 Hz with a lower cutoff frequency at 10 Hz. The LIGO (Laser Interferometric Gravitational-wave Observatory), GEO and VIRGO detectors have been undergoing constant improvements in their design and sensitivity. The advanced LIGO has about 10 folds increased sensitivity. They have now reached a sensitivity level where one can expect to detect gravitational wave with confidence and they are scheduled to be in operation in 2015.

1.4 Sources of Gravitational Waves

The detector output contains faint signals and there has been a lot of emphasis on developing efficient data analysis strategies. The data analysis

techniques are optimized depending on the nature of source. The sources that emit GW signals in the sensitivity band of LIGO and VIRGO detectors are roughly categorized into four groups.

- Compact Binary Coalescence
- Continuous Wave Sources
- Burst Sources
- Stochastic Gravitational Wave Source

This thesis concerns itself with the data-analysis techniques used for gravitational waves emitted during compact binary coalescence and by stochastic gravitational wave sources. Chapter 2 introduces the matched filtering technique used for searching compact binary Coalescence. Chapter 3, presents our study of how sine-Gaussian glitches effect the matched filtering operation. Chapter 4 builds a framework for stochastic gravitational wave map-making. In Chapter 5, we discuss the implementation of regularized deconvolution in the context of map-making.

Chapter 2

Compact Binary Coalescence

Compact binary systems are astrophysical systems comprising of two black holes and/or neutron stars orbiting around a common center of mass. A system of orbiting compact spherical masses has a time-varying quadrupole moment and will emit gravitational waves. As they lose energy, their orbits decay and the compact masses spiral inwards. Their orbital frequency increases and towards the final stage of their coalescence, their orbital frequency is very high. For a short time before colliding, the binary systems that lie in a suitable mass range, emit gravitational waves that fall in the sensitivity band of the LIGO detectors. This insprial phase is followed by a violent merger. After they undergo a merger, there is gravitational recoil and this phase is called as the ringdown phase.

The dynamics of orbital evolution of a inspriling compact binary system is relatively well understood. It is primarily driven by the loss of energy due to gravitational radiation. Functional form of the gravitational wave signals emitted during compact binary coalesces have been computed to a reasonable accuracy ([Blanchet et al., 2004]). Having prior knowledge on the signal waveforms offers a huge advantage in the data analysis. One can use pattern matching strategies like matched filtering to extract these signals. These sources are thus, promising candidates for the first direct detection ([Abadie et al., 2010]).

In this chapter, we shall briefly discuss the signal emitted during compact binary coalescence and the data analysis techniques associated with them. It aims at building the necessary framework required to describe the work presented in the next chapter.

2.1 Gravitational Waves Emitted During Compact Binary Coalescence

When the perturbations are small, one can use linearized Einstein's equation where the higher order terms in perturbation are ignored. The linearized Einstein's equations can be solved to obtain,

$$\bar{h}_{\alpha\beta}(t,\mathbf{x}) = 4\int d^3\mathbf{x}' \frac{[T^{\alpha\beta}(t',\mathbf{x}')]_{\mathbf{retarded-time}}}{|\mathbf{x}-\mathbf{x}'|} \tag{2.1}$$

Here $T^{\alpha\beta}$ is the energy-momentum tensor. For a far away non-relativistic source, this expression can be approximated to

$$\bar{h}_{\alpha\beta}(t,\mathbf{x}) \longrightarrow 2\frac{\ddot{I^{\alpha\beta}}(t-R)}{R} \tag{2.2}$$

Here, R is the distance of the source from the observer and $I^{\alpha\beta}$ is the second mass moment.

The eccentricities of the inspiraling binary orbits decay as they evolve. By the time GW signals emitted by the system enter the detector sensitivity bandwidth, their orbits are almost circular. Therefore, for our purposes we can consider their orbits to be circular with an instantaneous radius r(t). Let the instantaneous orbital frequency be $\omega(t)$. At this point, one has to notice that there are two timescales involved in this problem - the orbital period and the timescale over which the orbits shrink. The timescale over which the orbit shrinks is much larger than the orbital period and hence, one can use the adiabatic approximation to write down the trajectory of the masses as -

$$x(t) = rcos(\omega t) \tag{2.3}$$
$$y(t) = rsin(\omega t) \tag{2.4}$$
$$z(t) = 0 \tag{2.5}$$

The second mass moment of such a system is,

$$I^{xx} = \frac{1}{2}\mu r^2[1+cos(2\omega t)] \tag{2.6}$$
$$I^{xy} = \frac{1}{2}\mu r^2 sin(2\omega t) \tag{2.7}$$
$$I^{yy} = \frac{1}{2}\mu r^2[1-cos(2\omega t)] \tag{2.8}$$

Here, μ is the reduced mass of the system. For equal mass binaries, one can plug this in the linearized Einstein's equation and get,

$$\bar{h}^{\alpha\beta} = -\frac{8\omega^2 M r^2}{R} \begin{pmatrix} cos(2\omega(t-r)) & sin(2\omega(t-r)) & 0 \\ sin(2\omega(t-r)) & -cos(2\omega(t-r)) & 0 \\ 0 & 0 & 0 \end{pmatrix} \tag{2.9}$$

Notice that the frequency of gravitational waves emitted is twice their orbital frequency (i.e) $\omega_{GW} = 2\omega$. As the system losses energy, their orbital frequency increases and so does the frequency of emitted GW radiation. Also from the above equation, it is clear that amplitude of the radiation also increases. Thus, the GW signal emitted by an inspriling binary system increases in both amplitude and frequency over time and the waveform is popularly called as chirp. Figure 2.1 shows a typical chirp waveform.

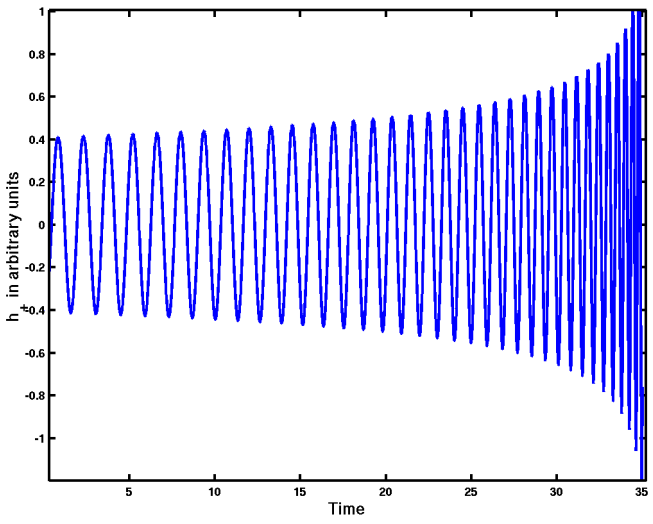

(a)

Figure 2.1: This figure shows a typical chirp signal. Notice that both amplitude and frequency of the signal increases with time.

Defining symmetric mass ratio as

$$\eta = \frac{\mu}{M_{total}} \tag{2.10}$$

And $\nu = r\omega_{GW}$ From Kepler's law,

$$GM_{total}\omega_{GW} = \nu^3 \tag{2.11}$$

Using virial theorem, the energy is given as ,

$$E = -\frac{1}{2}\mu\nu^2 \tag{2.12}$$

Gravitational wave luminosity is given by -

$$\mathcal{L}_{\mathcal{GW}} = \frac{32}{5}\eta^2\nu^{10} \tag{2.13}$$

Using $\mathcal{L}_{GW} = -\frac{dE}{dt}$, one can easily see that,

$$\frac{d\nu}{dt} = \frac{32\eta}{5M_{total}}\nu^9 \tag{2.14}$$

From this one can obtain -

$$t(\nu) = t_c - \frac{5}{256\eta}M_{total}\nu^{-8} \tag{2.15}$$

Further the phase (ϕ) evolution can be calculated as follows,

$$\frac{d\phi}{d\nu} = \frac{d\phi}{dt}\frac{dt}{d\nu} \tag{2.16}$$

$$\phi(\nu) = \phi_c - \frac{1}{32\eta}\nu^{-5} \tag{2.17}$$

Now, we again use $f_{GW} = \frac{\nu^3}{\pi M_{total}}$ and get the time-frequency relation as-

$$\frac{df}{dt} = \frac{96}{5}\pi^{8/3}\eta M_{total}^{5/3}f^{11/3} \tag{2.18}$$

A detailed derivation of the gravitational radiation from point masses in Neetonian limit is given in [Peters and Mathews, 1963].

2.2 The Technique of Matched Filtering

Detection of a signal concerns with deciding presence or absence of a known signal in a given detector output. According to Neyman Pearson lemma,

the likelihood ratio is an optimal detection statistic in presence of stationary Gaussian noise. It can be shown that likelihood function is directly proportional to the inner-product of detector output with the expected waveforms ([Mohanty and Dhurandhar, 1996]). The waveforms of signal emitted during inspiring phase have been accurately modeled and are commonly referred to as templates. Their inner product is defined in such a way that the contribution from different frequency components are inversely weighted with the detector noise power spectrum.

The inner product is defined as,

$$< \tilde{s}(f)|\tilde{h}(f) >= 2\int_{f_{\rm lower}}^{f_{\rm upper}} \frac{\tilde{s}(f)\tilde{h}^*(f) + \tilde{s}^*(f)\tilde{h}(f)}{S_h(f)}\, df\,. \tag{2.19}$$

Here, s(f) is the signal in the frequency domain and h(f) is the template. The function $S_h(f)$ is called the detector sensitivity curve and is the noise power spectrum of the detector. It is the Fourier transform of the auto-correlation function $N(\tau)$ of the detector n (t). The auto-correlation function captures the statistical property of detector noise.

$$N(\tau) =< n(t)n(t+\tau) > \tag{2.20}$$

In the Fourier domain,

$$S_h(f) = 2\int_{-\infty}^{\infty} N(\tau)e^{2\pi i f\tau}\, d\tau \tag{2.21}$$

Matched filtering is an operation of taking this inner product and is the optimal detection statistics when the signal waveform is known accurately. It compares the pattern present in the data against the modeled waveform. Match filtering takes the correlation $C(\tau)$, where τ is the time-lag between the signal and the template. The correlation $C(\tau)$ is given by

$$C(\tau) \;=\; \int_{f_{\rm lower}}^{f_{\rm upper}} \frac{\tilde{s}(f)\tilde{h}^*(f)}{S_h(f)} e^{2\pi i f\tau}\, df\,. \tag{2.22}$$

The integration is done from the lower cutoff frequency of the detector band width. The upper cutoff is generally taken as the frequency corresponding to inner most stable orbit.

2.3 An Introduction to Searches for Binary Coalescence

A very naive and simplified description of the compact binary search is discussed below. For a black hole binary system, the source parameters that effect the waveforms of the GW signal are the masses, orbital eccentricity and spins. A bank of templates that are optimally spaced in these parameters are constructed. A detailed discussion on optimal placement of templates can be found in [Owen, 1996, Sathyaprakash and Dhurandhar, 1991, Sathyaprakash and Schutz, 2009, Balasubramanian and Dhurandhar, 1998]. A matched filtering operation is performed on each of the detector outputs against these templates. The correlation output that crosses a certain threshold limit generates a trigger. If the trigger is found in more than one detector, they are considered to be candidates for true signals. A second round of matched filtering is performed on the coincident events and triggers are generated again. A next level of data analysis like veto analysis is performed on these, to establish absence or presence of signal. A more detailed description can be found in papers like [Messaritaki and LIGO Scientific Collaboration, 2005, Babak et al., 2013]

Chapter 3

Effect of sine-Gaussian Glitches on Searches for Binary Coalescence

A wide class of glitches that effected the search of compact binary coalescent in the first generation detector data can be modeled by sine-Gaussians. These glitches are known to produce spurious triggers and pose a threat of false detection ([Blackburn et al., 2008]). For a short stretch of insprial template where the frequency of template waveform matches the frequency of the sine-Gaussian glitches, a high correlation is obtained. It may raise the SNR large enough to exceed the trigger generating threshold. Further, one has to realize that these the triggers are generated at the coalesce time of the associated template. There is a delay between the time of occurrence of these glitch and the trigger. A crude way to deal with this is to neglect the whole stretch of data in the time-series that may contain the effect of the glitch. However, when one deals with long templates, this strategy is very inefficient.

A more detailed analysis of the on the trigger generated by these sine-Gaussian glitch becomes very important, especially with the advent of aLIGO ([Harry and the LIGO Scientific Collaboration, 2010]). Lowering the cutoff frequency to 10 Hz from 40 Hz will necessitate longer templates ([Allen et al., 2012]). In such cases, we find that the delay in the trigger can be as large as a few minutes. Given such circumstances, the ability to predict the exact time and nature of trigger generated will offer a huge advantage in vetoing false triggers. For instance, one could consider neglecting just a narrow window

in the time series where the trigger is expected to peak. With this motivation, we present a study on the effect sine-Gaussian glitches on the matched filtered search of coalescing binaries. Specifically, we develop approximate analytic expressions for the correlation $C(t)$ and validate it against numerical simulations. Using these expression one can obtain both amplitude and time-delay associated with these spurious triggers.

This work has been done in collaboration with Tito Dal Canton, Sanjeev Dhurandhar and Andrew Lundgren. It is currently in manuscript preparation stage.

3.1 Sine-Gaussian Glitches

In the following analysis, we consider a unit amplitude Sine-Gaussian glitch characterized by central frequency f_0 and quality factor Q,

$$s(t) = e^{-\frac{t^2}{\tau^2}} \sin(2\pi f_0 t)\,, \tag{3.1}$$

where, τ is the decay factor.

In the positive frequency domain, this translates to a Gaussian around f_0 given by,

$$\tilde{s}(f) = Ae^{-\pi^2\tau^2(f-f_0)^2}\,, \tag{3.2}$$

where,

$$A = \frac{1}{2i}\pi^{1/2}\frac{Q}{2\pi f_0}\,. \tag{3.3}$$

Defining the quality factor Q of the Sine-Gaussian as,

$$Q = 2\pi f_0 \tau\,, \tag{3.4}$$

the Sine-Gaussian can be expressed as,

$$\tilde{s}(f) = Ae^{-\frac{(f-f_0)^2Q^2}{4f_0^2}}\,. \tag{3.5}$$

Figure 3.1 depicts a typical sine-Gausian glitch.

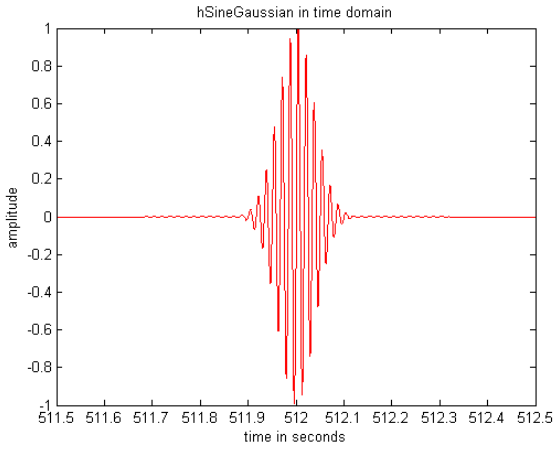

(a)

Figure 3.1: Sine-Gaussian Glitches : A unit amplitude sine-Gaussian glitch with a central frequency 60 Hz and the quality factor Q=20 is injected at the center of 1024 seconds long data segment, at 512 seconds.

3.2 Chirp Waveform

The Newtonian insprial binary template computed in the frequency space using stationary phase approximation (SPA) ([Sathyaprakash and Dhurandhar, 1991]) is given below.

$$\tilde{h}(f) = h_0 f^{\frac{-7}{6}} e^{-i\psi(f)} \,. \tag{3.6}$$

h_0 is the normalization constant. The phase $\psi(f)$ of the template is given by,

$$\psi(f) = 2\pi f t_c - \phi_c - \frac{\pi}{4} + \frac{3}{128}(\pi \mathcal{M} f)^{\frac{-5}{3}} \tag{3.7}$$

Here, $\mathcal{M}$ is the chirp mass of the binary system. We set t_c and ϕ_c to zero so that the chirp appears at the end of the time-series. The template is shown in Figure 3.2.

Further, we express the inspiral binary template in terms of a more convenient parameter - the chirp time τ_0 (as defined in [Sathyaprakash and Dhurandhar, 1991] and [Sengupta et al., 2002]) instead of chirp mass $\mathcal{M}$. When chirp time is used as a parameter to construct the template banks, the metric components in the parameter space are nearly constant. This implies that the templates are placed equidistantly and simplifies the analysis.

Physically, τ_0 is the time taken for a binary system to coalesce starting from a fiducial frequency f_a. Usually, in the literature, the fiducial frequency is taken to be the seismic cut-off frequency. When fiducial frequency is set to seismic cut-off frequency, τ_0 gives the duration of the signal that falls in the detector bandwidth.

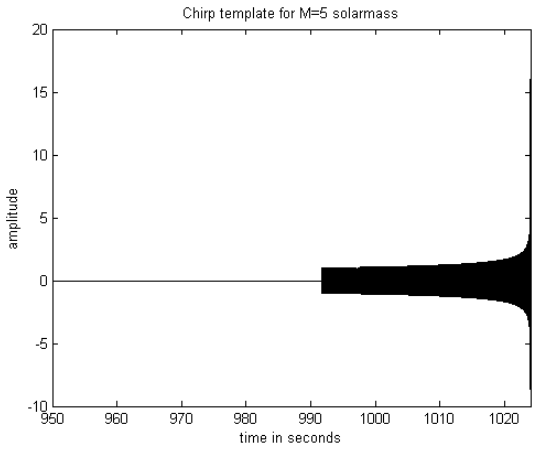

(a)

Figure 3.2: Chirp Waveform : An unnormalised binary inspiral chirp waveform is shown in this figure below. This template corresponds to $\mathcal{M} = 5\, M_\odot$. Note that only relevant segment of the data segment is shown in the figure.

However, the natural choice of fiducial frequency f_a in our analysis is not the seismic cut-off frequency . Here, a more appropriate choice of f_a is the central frequency of the Sine-Gaussian f_0. This is a natural choice because the correlation builds up only when the phase of the sine-Gaussian and the template match. Thus, we define τ_0 as

$$\begin{aligned} \tau_0 &= \frac{5}{256\pi\eta f_0}(\pi\mathcal{M}f_0)^{-5/3} \\ &= 11.72\left(\frac{f_0}{60Hz}\right)^{-8/3}\left(\frac{\mathcal{M}}{M_\odot}\right)^{-5/3}\text{sec}\,, \end{aligned} \tag{3.8}$$

where, $\eta = \mu/M$ and μ and M are the reduced and total mass of the binary respectively.

3.3 Effect of sine-Gaussian Glitches on Matched Filtering

We find three approximate analytical expression for the correlation. These approximation compliment each other and cover the whole parameter space. The parameters in our analysis is the central frequency f_0 and Q factor of the sine-Gaussian and chirp mass associated with the template $\mathcal{M}$.

3.3.1 Correlation

The matched filtering operation results in the complex correlation $C(t)$, where t denotes the time-lag parameter between the signal and the template. The statistic is $|C(t)|$. The correlation $C(t)$ is given by:

$$\begin{aligned} C(t) &= \int_{f_{\rm lower}}^{f_{\rm upper}} \frac{\tilde{s}(f)\tilde{h}^*(f)}{S_h(f)} e^{2\pi i f t}\, df\,, \\ &= \int_{f_{\rm lower}}^{f_{\rm upper}} \frac{\frac{1}{2}\pi^{1/2}\frac{Q}{2\pi f_0} e^{-\frac{(f-f0)^2 Q^2}{4f0^2}} h_0 f^{\frac{-7}{6}} e^{i\psi(f)}}{S_h(f)} e^{2\pi i f t}\, df\,. \end{aligned} \tag{3.9}$$

The range integration is from $f_{\rm lower} = 15$ Hz to $f_{\rm upper} = 500$ Hz. h_0 is the normalization constant of the template which is determined by,

$$\int_{f_{\rm lower}}^{f_{\rm upper}} \frac{|\tilde{h}(f)|^2}{S_h(f)}\, df = 1\,. \tag{3.10}$$

The correlation is inverse weighted by the zero detuning, low power sensitivity curve (from Ajith 2011) $S_h(f)$,

$$S_h(f) = (0.0152\frac{f}{245.4}^{-4} + 0.2935\frac{f}{245.4}^{\frac{9}{4}} + 2.7951\frac{f}{245.4}^{3/2} - 6.5080\frac{f}{245.4}^{\frac{3}{4}} + 17.7622)\,. \tag{3.11}$$

We are interested in finding the peak of $|C(t)|$. Specifically, we want to find the time at which the correlation peaks t_{max} and the amplitude of correlation peak $|C(t_{max})|$.

We begin with correlation integral,

$$\begin{aligned} C(t) &= \frac{Qh_0}{4i\sqrt{\pi}f_0}\int_{f_{lower}}^{f_{upper}} \frac{e^{-\frac{(f-f0)^2Q^2}{4f0^2}} e^{i\psi(f)+2\pi ift}}{f^{7/6}S_h(f)}\,df\,, \\ &= B\int \frac{e^{-\frac{(f-f0)^2Q^2}{4f0^2}} e^{i\phi(f)}}{f^{7/6}S_h(f)}\,df\,, \end{aligned} \tag{3.12}$$

where B anf ϕ are defined as follows,

$$B = \frac{Qh_0}{4i\sqrt{\pi}f_0} e^{\frac{-i\pi}{4}}\,, \tag{3.13}$$

and

$$\phi(f) = 2\pi ft + \frac{6\pi f_0\tau_0}{5}\left(\frac{f}{f_0}\right)^{-5/3}\,. \tag{3.14}$$

Note that this correlation integral does not have a exact analytical expression and one needs to use appropriate approximations.

3.3.2 Numerical Implementation

We model the response of matched filtering operation to validate our analytical approximations. The following is the range of integration considered in our analysis,

$$F_{min} = 15Hz \tag{3.15}$$

$$F_{max} = 500Hz \tag{3.16}$$

We consider a data train of length 512 seconds. A Nyquist frequency of 1024 Hz is set. Sine-Gaussian glitch of known central frequency and Q is injected in the middle of the data train at 256 second. This noiseless sine-Gaussian is then correlated with a Newtonian insprial template. The correlation is plotted in the time domain. The amplitude of correlation and time-delay between the injection of glitch are then compared to the analytical predictions.

The following define the parameter space we investigate. The central frequency of the sine-Gaussian ranges from $f_0 = 30$ Hz to 400 Hz. Q is varied from 5 to 20. The insprial template we use correspond to a mass range of $\mathcal{M} = 1.2\ M_\odot$ to $5\ M_\odot$

3.3.3 Approximation 1

Since the correlation integral has no exact analytical expression, we aim to simplify it using certain approximations. We can Taylor expand the phase term $\phi(f)$ up to quadratic order about some frequency f_1. In approximation 1, we choose f_1 to be the frequency f_s that corresponds to stationary point of phase. We obtain f_s by solving the equation,

$$\phi'(f_s) = 2\pi t - 2\pi\tau_0 \left(\frac{f_s}{\tau_0}\right)^{-8/3} \equiv 0\,, \tag{3.17}$$

Here, the prime denotes the derivative with respect to the argument. Thus,

$$f_s(t) = f_0 \left(\frac{t}{\tau_0}\right)^{-3/8}\,. \tag{3.18}$$

Notice that f_s is a fucntion of t.

Further, the phase $\phi(f)$ can be approximated as,

$$\phi(f) \simeq \phi(f_s) + \frac{1}{2}(f - f_s)^2\phi''(f_s)\,, \tag{3.19}$$

where,

$$\phi''(f_s) = \frac{16\pi\tau_0}{3f_0}\left(\frac{f_s}{f_0}\right)^{-11/3}\,. \tag{3.20}$$

Since $f^{-7/6}$ and $S_h(f)$ are slowly varying functions as compared to the numerator of the correlation integral over most regions of parameter space, we evaluate them at f_s. Using these approximations, the correlation integrand can be expressed as a product of real Gaussian centered at f_0 with standard deviation σ_{sg} and a complex Gaussian centered at f_s with a standard deviation σ_f.

The standard deviations of the Gaussians are as below,

$$\sigma_f(f_s(t)) = \frac{1}{\sqrt{\phi''(f_s)}} = \sqrt{\frac{3f_0}{16\pi\tau_0}}\left(\frac{f_s}{f_0}\right)^{11/6}\,, \tag{3.21}$$

$$\sigma_{sg} = \frac{\sqrt{2}f_0}{Q}\,. \tag{3.22}$$

The correlation integral can be expressed as,

$$C(t) = B\frac{1}{f_s^{\frac{7}{6}}S_h(f_s)}e^{i\phi(f_s)}\int_{f_{\text{lower}}}^{f_{\text{upper}}} e^{-\frac{(f-f0)^2}{2\sigma_{sg}}} e^{i\frac{(f-f_s)^2}{2\sigma_f}}\, df \tag{3.23}$$

$$= B\frac{1}{f_s^{\frac{7}{6}}S_h(f_s)}e^{i\phi(f_s)}J \tag{3.24}$$

We now define the following quantities,

$$\Delta f = f_0 - f_s(t) \tag{3.25}$$

$$x = \frac{f - f_0}{\sigma_{sg}} \tag{3.26}$$

$$\Sigma = \frac{\sigma_{sg}}{\sigma_f(t)} \tag{3.27}$$

$$\Delta = \frac{\Delta f}{\sigma_f} \tag{3.28}$$

At this point, one has to notice that except for Δf, all other quantities are dimensionless. Σ and Δ are functions of time through σ_f . Σ quantifies the ratio of the two standard deviations. In the correlation integral, we now switch to the dimensionless quantity x and complete the square.

$$J = \sigma_{sg}e^{i\frac{\Delta f^2}{2\sigma_f^2}} e^{-\frac{1}{2}\frac{\Delta^2\Sigma^2}{1-i\Sigma^2}} \int_{x_{\text{lower}}}^{x_{\text{upper}}} \exp - \left[\frac{1}{2}\left(\sqrt{1-i\Sigma^2}x - i\frac{\Sigma\Delta}{\sqrt{1-i\Sigma^2}}\right)^2\right] dx \tag{3.29}$$

Using Cauchy's theorem to appropriately shift contours in the complex plane we finally obtain,

$$J = \sigma_{sg}e^{i\frac{\Delta f^2}{2\sigma_f^2}} e^{-\frac{1}{2}\frac{\Delta^2\Sigma^2}{1-i\Sigma^2}} \frac{\sqrt{2\pi}}{\sqrt{R}} e^{-\frac{i\chi}{2}} \tag{3.30}$$

where,

$$R^2 = 1 + \Sigma^4, \qquad \tan\chi = -\Sigma^2\,. \tag{3.31}$$

Simplifying this leads us to our final expression of correlation $C(t)$.

$$|C(t)| = \frac{1}{2}\frac{h_0}{f_s^{7/6}(t)S_h(f_s(t))(1+\Sigma^4)^{1/4}} e^{-\frac{1}{2}\frac{\Delta^2\Sigma^2}{1+\Sigma^4}}\,. \tag{3.32}$$

We refer to this equation as approximation 1.

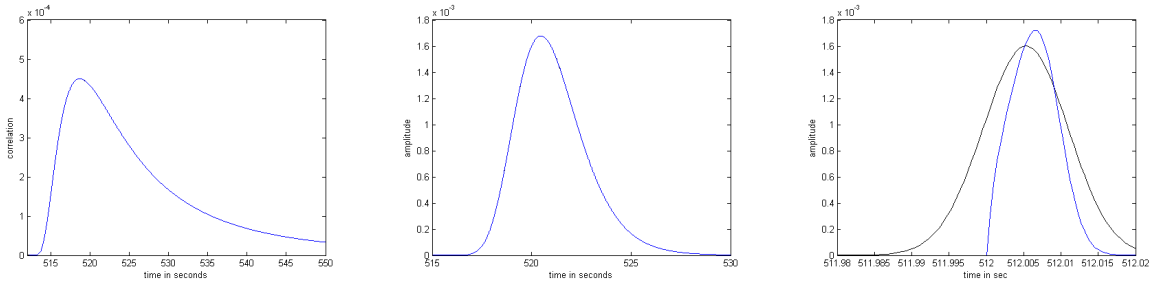

(a) f_0=60 Hz $\mathcal{M}$=1.2 $M_\odot$ Q=5 (b) f_0=60 Hz $\mathcal{M}$=1.2 $M_\odot$ Q=20 (c) f_0=400Hz $\mathcal{M}$=5 $M_\odot$ Q=5

Figure 3.3: Validating approximation 1 against numerical simulation : In the figures above, the blue curve depicts the analytic expression predicted by approximation 1. The black curve corresponds to the numerical simulation of the matched filtering operation. In figures (a) and (b) the blue and black curves are indistinguishable and thus the agreement is excellent. In (c) one can spot the difference but the difference is not too large. Thus, on a whole approximation 1 seems to work well. Sine-Gaussians with central frequency f_0 and quality factor Q have been injected symmetrically about the middle of the data segment at $t_{injection} = 512$ seconds in the time-series data segment of length 1024 second as shown in figure 1 (a). The sampling rate is 2048 Hz. The frequency range for integration is $f_{\text{lower}} = 15$ Hz to $f_{\text{upper}} = 500$ Hz.

This expression gives excellent result for the peak value of correlation and the time at which it occurs over most of the range of the parameter space. This has been exemplified in Figure 3.3

Despite of the fact that the predictions of the peak values and the time of occurrence of peak matches reasonably well with the numerical simulation for this approximation, we find that the shape of the correlation curve $C(t)$ does not always match well when σ_{sg} is comparable to σ_f. For instance, it can be seen in the sub-figure (c) that shape of the numerically obtained curve and the curve predicted by approximation 1 are do not overlap exactly. Here, $\sigma_f(f_s) \sim 70Hz$ and $\sigma_{sg} \sim 28Hz$. On the contrary, sub-figure (a) and (b) show that the predictions of this approximation exactly matches the numerical simulation when the value of $\sigma_{sg} \gg \sigma_f(f_s)$.

The expansion about the stationary point f_s works best when the function $\phi(f)$ has a deep minima. This means that stationary point should be sharply defined. In other words, the inverse of curvature of $\phi(f)$, σ_f should be small

around the stationary point for stationary phase approximation to be valid. In the region of parameter space where the function $\phi(f)$ has a very shallow minima, expanding the phase about f_s is no longer justified. We find that in such a situation, expanding phase about f_0 yields a more accurate result. Approximation 3 is based on this argument.

Another point that should be noted is that the correlation has a non-trivial dependence on t. Both fs and σ_f are time-dependent function. What complicates it evaluation is that the correlation is dependent on the PSD of the noise through $S_h(f)$. Hence, the time of occurrence of the correlation peak has to be found numerically. However, one must highlight that this expression, although complicated, models the correlation very well for a large parameter space.

3.3.4 Approximation 2

This approximation is a slightly different application of stationary phase approximation. We write the integral in the form,

$$C(t) = \int G(f) e^{i\Phi(f)}\, df\,, \tag{3.33}$$

where,

$$G(f) = \frac{h_0 A f_0^{\frac{-7}{6}}}{S_h(f_0)} e^{-\frac{(f-f_0)^2 Q^2}{4 f_0^2}}\,, \tag{3.34}$$

and,

$$\Phi(f) = 2\pi f t - \psi(f)\,. \tag{3.35}$$

f=f_s is the same stationary point as in approximation 1 and is given by Eq. (3.18). Evaluating the integral:

$$\begin{aligned} |C(t)| &\simeq G(f_s)\sqrt{\frac{2\pi}{\text{mod }\Phi''(f_s)}}\,, \\ &= \sqrt{\frac{3}{128\pi}}\frac{(t\tau_0)^{-1/4}}{f_0^{5/3}}\frac{h_0 Q}{S_h(f_s)} e^{-\frac{Q^2}{4}\left[1-\left(\frac{t}{\tau_0}\right)^{-3/8}\right]^2}\,. \end{aligned} \tag{3.36}$$

Again, this has a complicated dependence on t and hence the time at which the correlation peak needs to be calculated numerically.

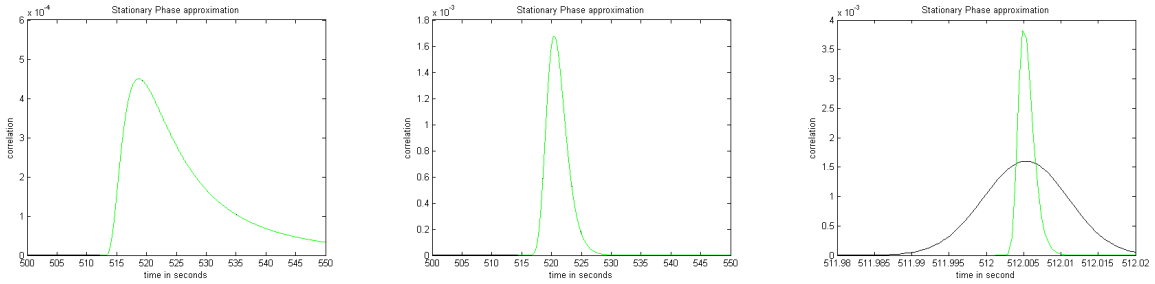

(a) f_0=60 Hz $\mathcal{M}$=1.2 $M_\odot$ Q=5 (b) f_0=60 Hz $\mathcal{M}$=1.2 $M_\odot$ Q=20 (c) f_0=400Hz $\mathcal{M}$=5 $M_\odot$ Q=5

Figure 3.4: Validating approximation 2 against numerical simulation : In the figures above, the green curve depicts the analytic prediction by approximation 2. The black curve corresponds to a numerical simulation of match filtering. Here again, the approximation matches very well in (a) and (b) but not in (c). At this point, one has to notice that approximation 1 gives a better result than approximation 2 for (c).

The results obtained using this approximation are shown in Figure 3.4.

We now show that approximation 2 can be obtained from approximation 1 in the regime $\sigma_{sg} \gg \sigma_f$ which is the same as $\Sigma \gg 1$. In such a case, approximation 1 can be written as,

$$\begin{aligned} |C(t)| &\simeq \frac{1}{2}\frac{h_0}{f_s^{7/6}S_h(f_s)\Sigma}e^{-\frac{1}{2}\frac{\Delta^2}{\Sigma^2}}, \\ &= \frac{1}{2}\sigma_f\frac{h_0 Q}{\sqrt{2}f_0 f_s^{7/6}S_h(f_s)}e^{-\frac{1}{2}\frac{\Delta^2}{\Sigma^2}}, \\ &= \sqrt{\frac{3}{128\pi}}\frac{f_0^{1/2}}{\tau_0^{1/2}}\frac{f_s^{2/3}}{f_0^{17/6}}\frac{h_0 Q}{S_h(f_s)}e^{-\frac{1}{2}\frac{(f_s-f_0)^2}{\Delta f^2}}. \end{aligned} \tag{3.37}$$

On simplifying the above expression, we indeed find that expression derived using approximation 1 reduces to that obtained by approximation 2.

$$|C(t)| = \sqrt{\frac{3}{128\pi}}\frac{(t\tau_0)^{-1/4}}{f_0^{5/3}}\frac{h_0 Q}{S_h(f_s)}e^{-\frac{Q^2}{4}\left[1-\left(\frac{t}{\tau_0}\right)^{-3/8}\right]^2} \tag{3.38}$$

We find that this approximation breaks down when $\Delta f \approx \sigma_f$. In such situations, $G(f)$ can no longer be approximated to a constant $G(f_s)$. This

happens because the Fourier transform of the Sine-Gaussian changes significantly over the range σ_f. Further, for high Q values, the assumption that integral is dominated by the region around f_s is no longer valid. However, it should be highlighted that the time delay estimated by this approximation is valid over almost the whole parameter space.

3.3.5 Approximation 3

This approximation is derived to deal with large Q limit and high $\mathcal{M}$. Although one might less often encounter this situation in real data, we investigate it for the sake of completeness. In this approximation, procedure we adopt is very similar to approximation 1. The difference lies in the fact that the phase is expanded about the central frequency of Sine-Gaussian f_0 instead of f_s. We consider that major contribution to the correlation integral come from a narrow band around f_0.

$$C(t) = \frac{h_0 A f_0^{\frac{-7}{6}}}{S_h(f_0)} \int_{f_{lower}}^{f_{upper}} e^{-\frac{(f-f_0)^2}{2\delta f^2}} e^{i\psi(f)} e^{2\pi i f t}\, df \tag{3.39}$$

We define the following dimensionless variable α as,

$$\alpha = \frac{3(\pi \mathcal{M} f_0)^{\frac{-5}{3}}}{128} = \frac{6}{5}\pi\tau_0 f_0^{8/3} \tag{3.40}$$

Expanding the $\psi(f)$ about $f0$ to quadratic order, we get

$$C(t) = \frac{h_0 A f_0^{\frac{-7}{6}}}{S_h(f_0)} \int e^{-\frac{(f-f_0)^2}{2\delta f^2}} e^{i\frac{-\pi}{4}} e^{i\alpha - \frac{5}{3} i \frac{\alpha(f-f_0)}{f_0} + i\frac{20}{9}\alpha\frac{(f-f_0)^2}{f_0^2}} e^{2\pi i f t}\, df \tag{3.41}$$

Let η be the constant term given by

$$\eta = \frac{h_0 A f_0^{\frac{-7}{6}} e^{i(\frac{-\pi}{4} + 2\pi f_0 t + \alpha)}}{S_h(f_0)} \tag{3.42}$$

Next, we simplifying the exponent Θ inside the integral by defining a dimensionless variable -

$$x = \frac{f - f_0}{f_0} \tag{3.43}$$

$$\Theta = i\alpha(\frac{-5}{3}x + \frac{20}{9}x^2) - \frac{(x^2Q^2)}{4} + 2\pi ixtf_0 \quad (3.44)$$

$$= (i\gamma - 1)\frac{x^2Q^2}{4} + 2\pi if_0x(t-\beta) \quad (3.45)$$

Here,

$$\beta = \frac{5}{3}\frac{\alpha}{2\pi f_0} \quad (3.46)$$

$$\gamma = \frac{20}{9}\frac{4}{Q^2}\alpha = \frac{32}{3}\frac{f_0\pi\tau_0}{Q^2} \quad (3.47)$$

Completing the square, we obtain

$$\Theta = (i\gamma - 1)\frac{x^2Q^2}{4} + 2\pi if_0x(t-\beta) + \frac{4\pi^2f_0^2}{Q^2(1-i\gamma)}(t-\beta)^2 - \frac{4\pi^2f_0^2}{Q^2(1-i\gamma)}(t-\beta)^2 \quad (3.48)$$

Putting them back in the correlation equation,

$$C(t) = \eta e^{\frac{-2\pi^2(t-\beta)^2\delta f^2}{1-i\gamma}} \int e^{(\frac{\sqrt{i\gamma-1}Qx}{2} + \frac{2\pi f_0^2(t-\beta)}{Q\sqrt{1-i\gamma}})^2}\, dx \quad (3.49)$$

Once again we use Cauchy theorem to simplify the integral. We define R as the real part of $1 - i\gamma$ (i.e)

$$R = \sqrt{1+\gamma^2} \quad (3.50)$$

One can calculate the final expression for correlation as,

$$C(t) = \eta e^{\frac{-2\pi^2(t-\beta)^2\delta f^2}{1-i\gamma}}(\frac{\sqrt{2\pi}\delta f}{\sqrt{R}}) \quad (3.51)$$

The results are illustrated in Figure 3.5.

3.4 Conclusion

In this work we have developed three approximate analytical forms for the correlation of sine-Gaussian glitch with the insprial template. These approximation compliment each other and cover the entire parameter space. This analysis has bearing on vetoing inspiral triggers associated with the sine-Gaussian glitches. Further, it should be highlighted that a sine-Gaussian glitch might generate trigger in multiple templates. We anticipate that using this analysis, a large number of false-detection can be reduced. However, a quantitative investigation on reduction in the number of false-alarm on implementing this analysis is yet to be done and would be interesting study.

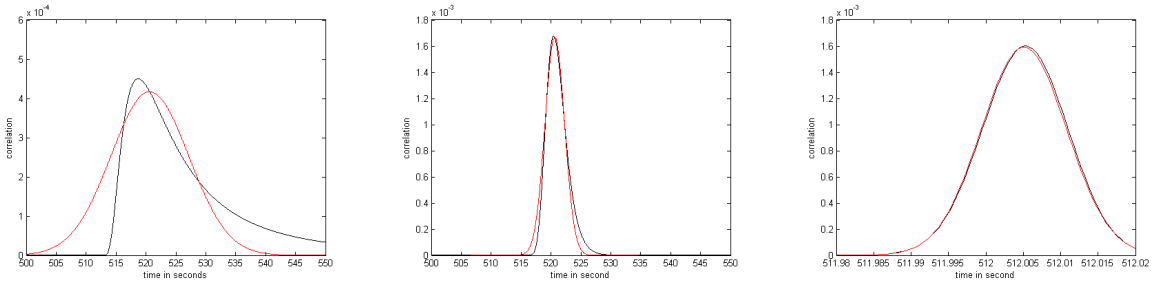

(a) f_0=60 Hz $\mathcal{M}$=1.2 $M_\odot$ Q=5 (b) f_0=60 Hz $\mathcal{M}$=1.2 $M_\odot$ Q=20 (c) f_0=400Hz $\mathcal{M}$=5 $M_\odot$ Q=5

Figure 3.5: Validating 0th order approximation against numerical simulation: In the figures above, the red curve depicts the analytic approximation predicted by 0th order approximation. The black curve corresponds to the numerical simulation of match filtering.The rest of the condition are similar to that described in Figure 2

Chapter 4

Stochastic Gravitational Wave Background

Unresolved astrophysical sources that produce gravitational waves by independent processes and gravitational radiation from cosmological origin constitute the stochastic gravitational wave background (SGWB). These are weak signals but their strength builds up when statistically averaged over a sufficiently long observation time. A general discussion on SGWB can be found in literature like [Allen and Romano, 1999, Allen and Ottewill, 1997]. The time averaged signals from SGWB can be used to build a sky map.

4.1 Radiometry

The technique of radiometry or aperture synthesis is used to make SGWB sky maps. A schematic diagram of a radiometer is shown in Fogure 4.1. The basic assumption here is that the noise in the two detectors will be independent while the gravitational wave signal will be correlated. It essentially involves cross-correlating signals received by a pair of detectors separated by a baseline length. When the phase of the signal received at the two detectors match, the signal builds up. Because of the geometric separation between the two detectors, the signal is received with a relative time delay. The time delay is a function of the effective baseline length and the source direction. The effective baseline length changes as the earth rotates and this phenomenon is used for aperture synthesis. The signals from the direction that correspond

to zero time-lag interfere constructively and the detector pair is said to be 'pointing in' this direction. The signal from all other direction statistically cancel out and do not contribute to the cross-correlation statistic. A pair of detectors can be made to point in any particular direction by artificially compensating the time-delay before carrying out the cross-correlation. To construct a SGWB map of the whole sky, the sky is divided into pixels and radiometry is performed on each of these pixels.

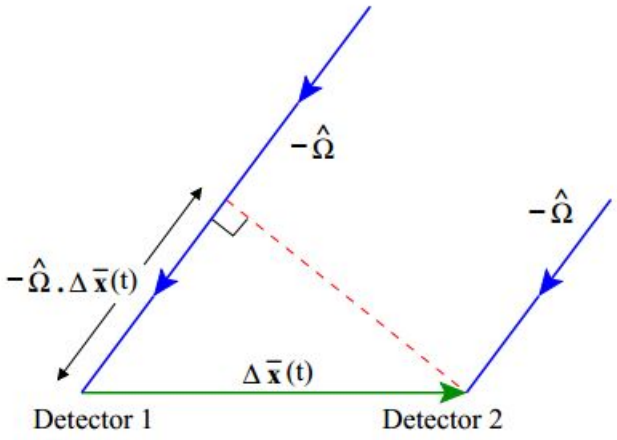

(a)

Figure 4.1: Radiometry : This figure is taken from [Mitra et al., 2008]. This figure depicts a basic radiometry setup. The seperation between the two detectors introduces a phase-lag and by compensating this appropriately, we can point the radiometer to any desired location in the sky.

4.2 The Beam and SGWB map-making

The total observation time T is broken into smaller time segment Δt in order to optimize the signal to noise ratio. Time ordered short-term fourier transform (SFT) is computed for each of these segments.

$$\tilde{X}_I(t;f) = \int_{t+\Delta T/2}^{t-\Delta T/2} X_I(\tau) e^{-2\pi i f \tau}\, d\tau\,. \tag{4.1}$$

An optimum cross-correlation statistic S(t) is obtained by using direction depndent filter function $\tilde{Q}(t,f)$ for each of these individual smaller time

segments.

$$s(t) = \int_{\infty}^{-\infty} \tilde{X}_1^*(t;f)\tilde{X}_2(t;f)\tilde{Q}(t,f)\,df\,. \tag{4.2}$$

The filter function is given as,

$$\tilde{Q}(t,f) = \lambda(t)\frac{H(f)\gamma^*(t,f,\hat{\Omega})}{P_1(t;|f|)P_2(t;|f|)} \tag{4.3}$$

Where H(f) is the frequency power spectrum of the source and $P_{1,2}(t;|f|)$ are the one-sided power spectral density of detector noise. $\gamma^*(t,f,\hat{\Omega})$ is the overlap reduction function that contains the information of relative orientation and the time delay between the detectors. The form of overlap function is given in [Flanagan, 1993]

$$\gamma^*(t,f,\hat{\Omega}) = \Gamma(\hat{\Omega},t,f)e^{2\pi i f\hat{\Omega}.\Delta x(t)/c} \tag{4.4}$$

$\Delta x(t) = x_2(t) - x_1(t)$ is the geometrical seperation and

$$\Gamma(\hat{\Omega},t,f) = \sum_A F_1^A(\hat{\Omega},t)F_2^A(\hat{\Omega},t) \tag{4.5}$$

The polarization are denoted A = $\{+,\times\}$ and $F_{1,2}^A(\hat{\Omega},t)$ is the antenna function.

The filter function is used to adjust the phase lag between the two detector outputs and point the radiometer to a desired patch (in the direction Ω)in the sky. The statistic developed over these smaller time segments are then linearly combined to obtain the final statistic for the whole observation time for each patch in the sky. This linear combination is done in such a way that the contribution from each segment is weighted by the inverse of its variance. This ensures a lower contribution from the noisy time segments. The statistic developed on each patch is then put together to make a sky map.

The map generated in this way is sky 'seen' through the detectors. The true sky signal is convolved with the response function (also called as the beam pattern of the detector) and this introduces a non trivial pixel-to - pixel covariance. The beam pattern captures the effect that a source in the direction $\hat{\Omega}$ has on an observation in the direction $\hat{\Omega}'$. Convolution equation is of form,

$$D(\hat{\Omega}) = \int d\hat{\Omega}' B(\hat{\Omega},\hat{\Omega}')S(\hat{\Omega}') + n(\hat{\Omega}) \tag{4.6}$$

The functional form of the beam pattern B is derived in [Mitra et al., 2008] and is,

$$B(\hat{\Omega},\hat{\Omega}') = \Lambda(\hat{\Omega}) \int dt \int_{\infty}^{-\infty} \frac{H(f)H'(f)}{P_1(t;|f|)P_2(t;|f|)} \Gamma(\hat{\Omega}',t,f)\Gamma(\hat{\Omega},t,f)e^{-2\pi i f\hat{\Omega}.\Delta x(t)/c}\, df\ . \tag{4.7}$$

Gravitational wave detector network has a beam pattern that extends over a large area in sky. The effect of the beam on a point source is illustrated in the Figure 4.2. Further, the smearing pattern of a point source depends on its location in the sky.

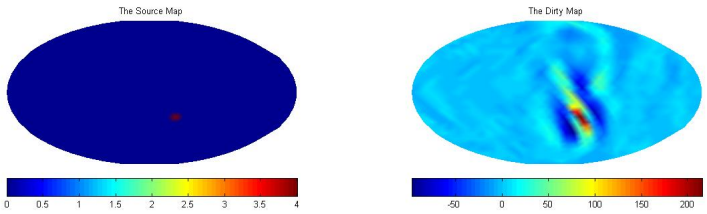

(a) Source Map (b) Dirty Map

Figure 4.2: Effect of the detector beam on a point source : The left panel shows the true sky map and the right panel shows the true sky convolved with detector beam. In these figures the colorbar indicates the intensity of the pixels.

4.3 Statistical Properties of Signal and Noise

SGWB signals are assumed to be stochastic and uncorrelated, both in frequencies and dirrections. Further, SGWB signal are also assumed to be gaussian random processes and that the second-order moments $< \tilde{h}^*(f,\hat{\Omega})\tilde{h}^*(f',\hat{\Omega}') >$ are sufficient to describe their statistical properties completely.

Statistical properties of the signal can be infered by the correlation function which is given as [Mitra et al., 2008, Allen and Romano, 1999]

$$< \tilde{h}^*(f,\hat{\Omega})\tilde{h}^*(f',\hat{\Omega}') >= \delta(f-f')\delta^2(\Omega-\Omega')P(\hat{\Omega})H(f) \tag{4.8}$$

The noise across the pixels in the dirty map is assumed to have a Gaussian probability distribution with a zero mean. However, it has a non-trivial pixel-to-pixel covariance matrix as a result of radiometry technique. The pixel-to-pixel noise covariance matrix happens to be equal to the beam matrix up to a factor of scalar constant [Mitra et al., 2008]

$$\langle n \rangle = 0 \tag{4.9}$$

And,

$$N = \langle n n^T \rangle \sim \mathbf{b} \tag{4.10}$$

Here, $\mathbf{b}$ is the symmetrized beam pattern.

Chapter 5

Probing Anisotropy of Stochastic gravitational wave background using prior knowledge on source distribution

The map constructed directly from the detector output contains the effect introduced by the detector response function and is not a true sky representation. A true signal S is observed as data D and is the result of convolution of the beam pattern (also called as response function) B with the signal S. The map also contains a Gaussian random noise n with covariance matrix N. In pixel basis, the above mentioned convolution equation simplifies to a set of linear expressions,

$$D = BS + n \tag{5.1}$$

Where D is the detector output vector such that D_i contains intensity observed at i^{th} pixel. In the context of map making, D is often referred as dirty map, S as source map and the recovered signal $\hat{S}$ which is an estimate of true sky is called cleaned map. To obtain a true sky representation from the dirty map, one has to undo the effects introduced by the beam pattern and this process is known as deconvolution.

However, the deconvolution of SGWB maps is not trivial because of the ill posed nature of the detector beam. The weakness of gravitational waves signals further complicates this problem, as the effect of noise becomes very

crucial for weak signals. For instance, one cannot undo the convolution effect of the beam by direct inversion of the beam.

$$\hat{S} = B^{-1}D \tag{5.2}$$

Doing so boosts the noise associated with the low sensitivity modes of detector beam. This results in a sky reconstruction dominated by noise. It has been demonstrate in the panel (d) of Figure 5.1. The only exception to this is when the source is the unrealistically strong.

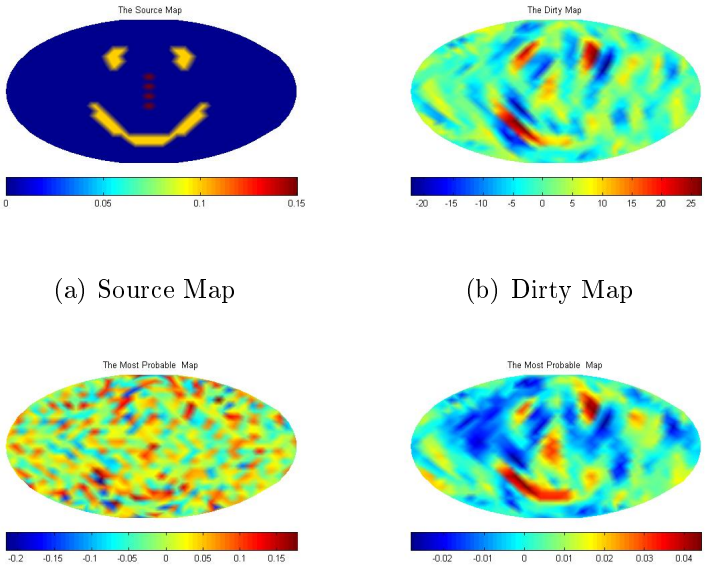

(a) Source Map

(b) Dirty Map

(c) Reconstruction by Direct Inversion

(d) Regularized Reconstruction

Figure 5.1: **Regularized Deconvolution**. The problem of deconvolution in SGWB is not trivial. Multiplying the inverse of the detector beam to undo its effect introduces noise. One generally casts this problem as a set of linear equations and then finds the clean map as a solution to them.

In this chapter, we show that implementing regularization along with deconvolution greatly helps to reproduce sky map faithfully. For instance, from panel (c) of the Figure 5.1, one can clearly see the merits of regularized deconvolution. We develop the formalism for regularized deconvolution in a Bayesian framework.

5.1 Bayesian Analysis

5.1.1 Most Likely Solution S_{ml}

Map-making deals with recovering the true signal from the detector output given the statistical properties of the noise n. In a Bayesian framework, this translates to finding the signal that maximizes the probability of obtaining the given detector output. When noise has a Gaussian probability distribution, as in the case of GW map making, one can express this mathematically as

$$P(D|S,B) = Z_L e^{-\frac{1}{2}(BS-D)^T N^{-1}(BS-D)} \tag{5.3}$$

This function is called as likelihood function and Z_L is the normalization constant. The signal that maximizes likelihood function is called the most likely solution S_{ml}.

One can recognize the exponential part of the likelihood function as negative of the well-known χ^2 estimator. χ^2 is used to estimate the goodness-of-fit of the data to the model. In terms of χ^2, the likelihood function can be expressed as,

$$P(D|S,B) = \frac{1}{Z_L} e^{-\frac{1}{2}\chi^2} \tag{5.4}$$

This leads to an alternative interpretation of S_{ml} as the solution that minimizes the χ^2. S_{ml} is thus, the best fit solution to the set of linear equations describing convolution.

$$\nabla\chi^2(S_{ml}) = 0 \tag{5.5}$$

This gives,

$$S_{ml} = (B^T N^{-1} B)^{-1}(B^T N^{-1} D) = B^{-1} D \tag{5.6}$$

5.1.2 Ill-Posed Problem and Regularization

Likelihood maximization in context of SGWB map-making turns out to be an ill posed problem. The GW detector beam matrix has a large number of singular values that are very closed to zero and thus, inversion of the beam matrix is non-trivial. A plot of singluar values of the detector beam is shown in Figure 5.2. Physically, this means that the detector network is insensitive to certain directions in sky. The information contained in the detector output

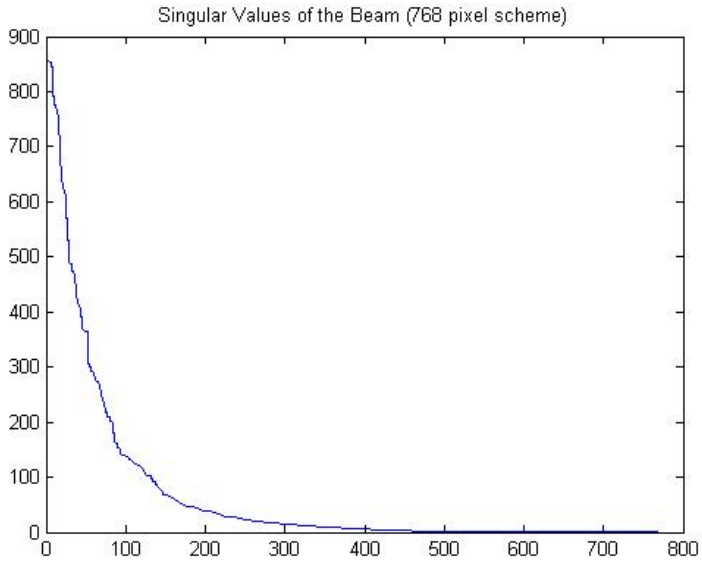

(a)

Figure 5.2: Singular values of the Beam (768 Pixels Resolution): The ill-posed-ness of the system is directly related to difference between the highest and the lowest singular values. Notice that a large number of singular values are close to zero. Very small singular values in the graph indicates the insensitivity of the detector to those modes.

is not sufficient to establish a unique one-to-one mapping between the true signal and the dirty map.

Another perspective to this problem can be obtained by looking at the χ^2 estimator. The set of linear equations that describe deconvolution, are not independent and thus, the problem has an ill-posed nature. Number of free parameters in the problem are much more that the number of constraint equations. This invokes the risk of over-fitting by minimizing χ^2 to an unrealistically small value. In an optimal case, χ^2 should attain a value close to the number of degrees of freedom in the problem. Thus, minimum χ^2 solution is not the best estimate of the true sky signal.

Problems of this nature exist in many fields and the well known way to tackle it is to implement regularization. For instance, one could find regularized image reconstruction used in gravitational strong lensing in ([Warren and Dye, 2003, Brewer and Lewis, 2006, Suyu et al., 2006]). The problem one deals in reconstructing sources in strong gravitational lensing is slightly

more complicated than our case, as the convolution kernel (lens potential) itself is not fully known.

Regularization provides additional information on the true sky signal. Generally, regularization functions are such that they penalize the solutions that differ from what is already known of the true signal. From the χ^2 perspective, regularization serves as a set of additional constraints and prevents data over-fitting.

5.1.3 Most Probable Solution S_{mp}

In a Bayesian framework, regularization is incorporated through prior. A prior distribution function gives the probability of true signal being S, if we choose to incorporate some addition information on the signal in form of a function R(S). Given R(S) and regularization strength λ, the prior distribution can be written as,

$$P(S|R(S),\lambda) = \frac{1}{Z_r} e^{-\lambda R(S)} \tag{5.7}$$

where Z_r is the normalization constant.

Using Bayes theorem, the posterior probability of getting the signal S, given the detector output D , the beam B and regularization function R(S) is given as follows,

$$P(S|D,B,\lambda,R(S)) = \frac{P(D|S,B)P(S|R(s),\lambda)}{P(D|\lambda,B,R(S)} \tag{5.8}$$

The posterior probability is the product of likelihood and the prior divided by the normalization function called evidence. Unlike in case of likelihood which depends only on data, posterior probability distribution evaluates the probability with which a given solution S could be the true signal by combining the observation (detector output) with what is already known about the true signal.

$$P(S|D,B,\lambda,R(S)) = \frac{1}{Z_P} e^{-M(S)} \tag{5.9}$$

Where M(S) is defined as,

$$M(S) := \chi^2(S) + \lambda R(S) \tag{5.10}$$

Most probable solution S_{mp} is obtained by maximizing the posterior probability with respect to S. The function M(S) contains two competing function - χ^2 and R(S). The most probable solution minimizes the a linear combination of these functions.

For our analysis, we construct R(S) as quadratic functions in S. Choosing a quadratic form of the regularization function ensures that the operations on the dirty map is always linear. This offers simplicity in terms of formulation and is also computationally less expensive. At this point, it should also be mentioned that a non-quadratic form of regularization like maximum entropy formulation, although complicated and computationally expensive, offer other kinds of advantages. For instance, a quadratic regularization function does not impose positivity of the source intensity as a prior. In fact, having quadratic form implies that positive and negative intensities are equally likely. The regularization functions we use are such that they favor a smooth reconstruction which contains as little source structure as possible. Say, the regularization function attains a minima at S_{reg}. We set $S_{reg} = 0$ to incorporate the condition of Occam's razor. This implies a prior preference to blank sky and helps in suppressing the noise.

$$\nabla(\chi^2(S_{mp}) + \lambda R(S_{mp})) = 0 \tag{5.11}$$

This gives the expression for S_{mp} as,

$$S_{mp} = (B + \lambda C)^{-1} D \tag{5.12}$$

Here, C is the hessian of R(S), i.e $C = \nabla\nabla R(S)$. From the above equation, regularization can be also be viewed as modifying the convolution kernel such that the problem becomes less ill-posed.

In summary, it should be noted that the reconstruction of source map without a prior corresponds to evaluating the expression for S_{ml} while regularized deconvolution corresponds to finding S_{mp}.

5.1.4 Strength of Regularization

The strength of regularization λ decides the balance between the goodness-of-fit and bias towards our prior knowledge. While low values of λ increase the

risk of over fitting the data, setting λ to large numbers will give us a highly biased solution. Setting a very high value for λ ensures that the solution is consistent with our prior knowledge, but it might have very little to do with the actual detector output. Thus, tuning λ to attain an optimal balance is crucial to obtaining reliable solution.

Besides the obvious dependence on the beam matrix, optimal value of λ also depends on the data itself. For instance, if the data contains a very strong source, low strength of regularization would suffice. On the contrary, if the source is weak and is highly contaminated by noise, a higher strength of regularization would be needed for a good reconstruction of the sky.

To find the optimal strength of regularization, we follow the formalism presented in ([Suyu et al., 2006]). The optimal strength for regularization is found by maximizing $P(\lambda|D, B, R(S))$ with respect to λ. Bayes rule tells us that,

$$P(\lambda|D, B, R(S)) = \frac{P(D|\lambda, B, R(S))P(\lambda)}{P(D|R(S), B)} \tag{5.13}$$

Since the order of magnitude of λ is unknown, a uniform prior in log λ is assumed. The denominator of the above expression is independent in lambda. This implies,

$$P(D|\lambda, B, R(S)) \propto P(D|\lambda, B, R(S)) \tag{5.14}$$

Further, $P(D|\lambda, B, R(S))$ can be identified as the evidence. Finding the optimal value of λ boils down to maximizing evidence with respect to log λ.

$$\frac{d}{dlog\lambda}(logP(D|\lambda, B, R(S)) = 0 \tag{5.15}$$

For $S_{reg} = 0$, this gives a non-linear equation whose solution corresponds to optimal value of λ. This equation is non-linear in λ but can be solved numerically by methods like bisection.

$$2\hat{\lambda}_{optimal}R(S_{mp}) = N_{pixels} - \hat{\lambda}_{optimal}Tr((B + \hat{\lambda}C)^{-1}C) \tag{5.16}$$

Where N_{pixels} is the number of pixels in the source map.

5.2 Quantifying the Quality of Reconstruction - Normalised Scalar Product (NSP)

In order to have noise suppression effect a prior preference towards blank sky is chosen. The cost associated with this is that the reconstructed map is biased towards minimum power (sum of intensities squared) solutions. It often happen that there is a huge difference in the amount of power contained in the dirty map and the cleaned map. In such cases, the usual estimators like root mean squared error (RMS) may not be a reliable estimator.

Since we aim at restoring the structures and patterns of the true sky rather than intensity at each pixel, it is useful to quantify amount of structural similarity between the reconstructed map and the true source map. One can express the map as a vector of dimension equal to the number of pixels. A simple estimator to do measure the similarity is the scalar product between normalize source map vector ($\hat{S_{true}}$) and normalize reconstructed map ($\hat{S_{clean}}$) vector. This quantifies the extent of overlap between the two maps. Higher the value of normalised scalar product (NSP), better is the quality of deconvolution.

$$NSP = \hat{S}_{clean}.\hat{S}_{true} \tag{5.17}$$

5.3 Numerical Implementation of Regularized Deconvolution

The following procedure is employed in our analysis. Sources are injected at desired pixels in the map to generate a source map. A dirty map is simulated from this source map by convolving it with the symmetrized GW detector beam given in [Mitra et al., 2008]. A Gaussian noise with appropriate statistical properties is added to it. This dirty map serves as the detector output vector and we aim to accurately estimate the pattern in the source map from this. We implement Bayesian regularization and compared to the true source map to the reconstructed map. The quality of reconstruction is quantified by NSP.

5.3.1 Pixelization Scheme

The sky is divided into pixels using Hierarchical, Equal Area, and iso-Latitude Pixelisation (HEALPix) scheme [Górski et al., 2005]. The resolution of the maps are set using the HEALPix parameter N_{side}. The total number of pixels N_{Pixels} in the maps are related to N_{side} as $N_{Pixels} = 12N_{side}^2$. We use $N_{side} = 8$ to generate our maps and in this resolution the sky is divided into 768 pixels.

5.3.2 Simulating Source Map

The sky is pixelized into 768 patches. The source is inject at a desired location to produce a source map. We simulate three main kind of source for our study - point source, extended diffused source and localized broad source.

The signal is integrated over a period of one day (approx. 86400 s). However, in reality, the integration time is generally much longer than this and thus, one can expect the signal strength to be higher. To give a rough idea of the signal strenght used in our study, we present a graph of the source power spectrum versus the detector power spectrum for a typical simulated source in Figure 5.3.

5.3.3 Quadratic Regularization function

The formalism described above is valid for any quadratic form of regularization function. In our analysis, we choose to investigate the effect of gradient minimization on source reconstruction. Following is the forms of regularization function used in our analysis -

- Gradient Regularization
  Gradient regularization incorporates a preference to smooth source reconstruction by penalizing the intensity difference between two neighboring pixels. It prefers minimum variation of intensities in the reconstructed map. The gradient across the reconstructed map is minimized

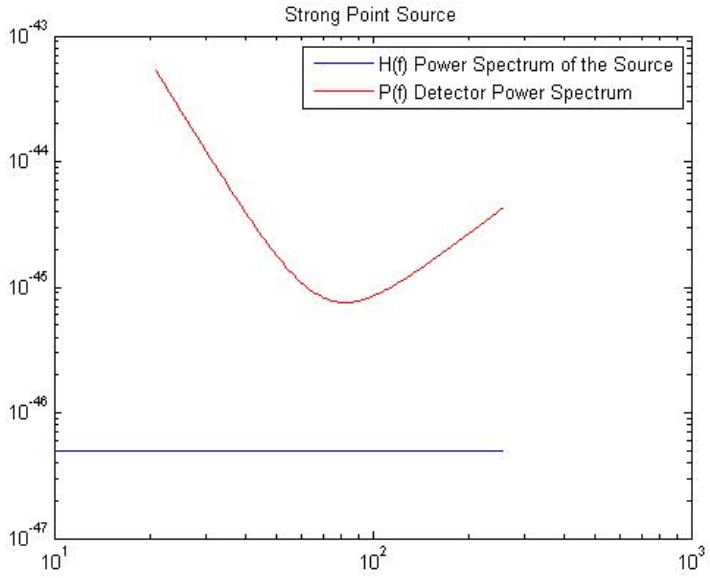

(a)

Figure 5.3: Power Spectrum of the Source Distribution and the detector : This figure compares the detector power spectrum with the power spectrum of a typical source we simulate for our analysis. The red curve corresponds to the detector power specturm and the blue line corresponds to power spectrum of the source. It indicates the strength of the source we use.

by using the following form of regularization.

$$R_{gradient}(S) = \sum_{i=1}^{No.ofPixels} \sum_{N_{ij}=N_{i1}}^{N_{i8}} (S_i - S_j)^2 s \tag{5.18}$$

Where N_{ij}indicates the j^{th} nearest neighbor to i^{th} pixel.

5.3.4 Computing S_{ml} and S_{mp}

Matrix inversions used in computing S_{ml} and S_{mp} are not numerically well-defined and hence, a direct inversion is not reliable. The numerical error on direct inversion for the matrix B happens to be very large. As an alternative, we formulate them into system of linear equations and solve them using suitable linear equation solver. In our implementation, we formulate the expression into a set of linear equations and solve for solve for S_{ml} and

S_{mp}. We use MATLAB's in-built solver cgs(), which uses modified conjugate gradient method to solve the below equation.

$$D = BS_{ml} \tag{5.19}$$

$$D = (B + \lambda C)S_{mp} \tag{5.20}$$

5.3.5 Calculating the Hessian Matrix C

C is the hessian of the regularization function R(S) and plays a very important role in reconstruction. It is an indicator of how sensitive the regularization function R(S) is to change in S. It is defined as,

$$C_{ij} := \frac{\partial}{\partial S_i}\frac{\partial}{\partial S_j}R(S) \tag{5.21}$$

For gradient regularization, one can compute C as-

$$C(i,j) = 2(N_\eta(i))\delta_{ij} - 2\delta_{j\eta_i} \tag{5.22}$$

Here, η_i denotes pixels neighboring i^{th} pixel and $N_\eta(i)$ is the number of neighbors of i^{th} pixel. Because of the choice of the pixelization scheme, each pixel has either 7 or 8 neighbors.

5.4 Results of Source Reconstruction using Gradient Regularization

As a demonstration, we show the results of source reconstruction for 5 different source intensity distribution. In first three cases the strength of the source is weak and regularization helps the reconstruction. The last two cases demonstrate two extreme scenarios - a very bright source and an extremely weak source. In these two cases, blind regularization does not offer much benefit.

Source Description	Regularization Strength that corresponds to Max. NSP	Regularization Strength calculated using Bayesian Inference	NSP for Regularized Deconvolution	NSP for Unregularized Deconvolution	Norm of the Source Map
9 Pixels Wide source	40	49.23	0.65	0.36	1.2
Point Source	10	Does not converge	0.3	0.2	1
Diffused Source	20	31.43	0.66	0.42	1.46
Very Strong Point Source	3	4.79	0.56	0.53	4
Very Weak Diffused Source	30	Does not converge	0.32	0.13	0.36

(a)

Figure 5.4: This table summarizes the quantitative results obtained on implementing gradient regularization.The norm of source map indicates the signal strength. The first three rows contain results from the cases where regularization helps to improve the reconstruction greatly. The fourth row shows that regularization is unnecessary for very strong source. The fifth row corresponds to a very weak signal and one sees that blind regularization is not sufficient for the reliable reconstruction.

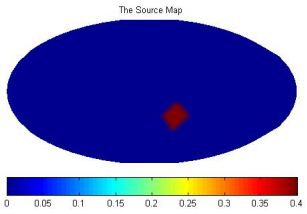

(a) Source Map

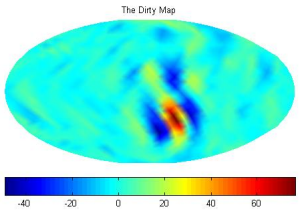

(b) Dirty Map

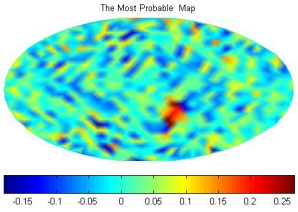

(c) Reconstruction without Regularization

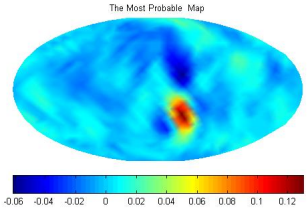

(d) Regularized Reconstruction

Figure 5.5: A Weak 9-pixels-wide source : In these figures the colorbar indicates the intensity of the pixels. When the source is weak, regularization helps the reconstruction greatly. From the panel (c) and (d) one can clearly see the improvement brought by regularization. The regularization strength used here is $\lambda = 40$

5.5 Source Reconstruction Using Prior Knowledge on Source Location

In many instances, some information about the stochastic gravitational source location is known through electromagnetic observation. Incorporating this information, offers an enormous advantage, especially if we are reconstructing faint sources from noisy data.

The most natural way of incorporating the source location is by constructing a regularization function of the following form -

$$R_{norm}(S) = \sum_{i=1}^{No.of Pixels} [S(i) - S_{model}(i)]^2 \tag{5.23}$$

Where S_{model} is the prior map that contains the information on the source

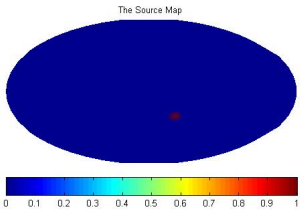

(a) Source Map

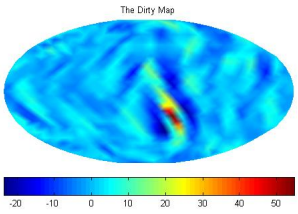

(b) Dirty Map

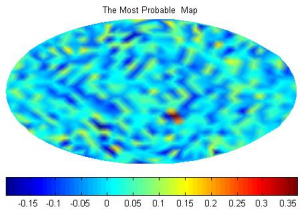

(c) Reconstruction without Regularization

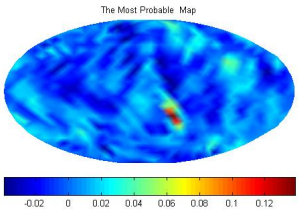

(d) Regularized Reconstruction

Figure 5.6: A Point Source : From the panel (c) and (d) one can clearly see the improvement brought regularization. Here we use $\lambda = 10$

location. This function penalizes the difference between the reconstructed map and the prior map. However, the one encounters a serious problem when using this form of regularization. The biases introduced by the prior map is very large and one finds that signal is picked up even from a pure noise map. Figure 5.10 depicts our attempt to use this functional form of regularization.

To reduced this problem of false alarm, we construct an alternative form of regularization function -

$$R(S) = \sum_{i=1}^{N_{Pixels}} [\frac{|S(i)|^2}{|S_{model}(i) + \kappa|} \tag{5.24}$$

Essentially, we modify the norm regularization function in such a way that penalty per pixel is inverse weighted by the intensity of that pixel in the prior map. This ensures that the reconstructed map is penalized less for pixel-intensities where we expect the source to be present. The factor κ in the above function is an ad-hoc factor. This factor relates to the maximum

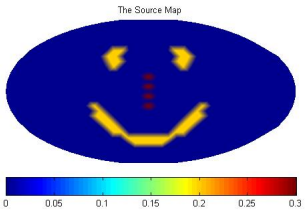

(a) Source Map

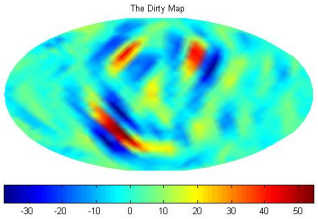

(b) Dirty Map

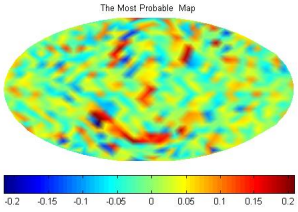

(c) Reconstruction without Regularization

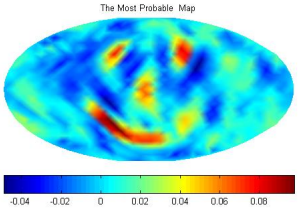

(d) Regularized Reconstruction

Figure 5.7: Diffused Source : The regularization strength used here is $\lambda = 20$. Here again, one can see the improvement brought by incorporating regularized deconvolution.

uncertainty expected in the intensity of the prior map. It is set to 10^{-2} in our analysis. We find that setting $\kappa = 10^{-2}$ does not pick up the signal from pure noise map but picks up the signal if the data actually has a weak signal resembling the prior map. The most probable map in this case becomes,

$$S_{mp} = (B + \mu C)^{-1} D \tag{5.25}$$

Where,

$$C(i,j) \approx \delta_{ij} \frac{1}{S_{model}(i) + \kappa} \tag{5.26}$$

The regularization constant is denoted as μ . This result obtained by this form of regularization function is shown in Figure 5.11.

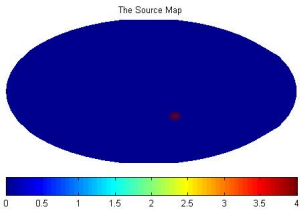

(a) Source Map

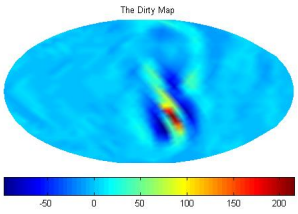

(b) Dirty Map

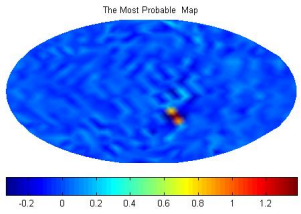

(c) Reconstruction without Regularization

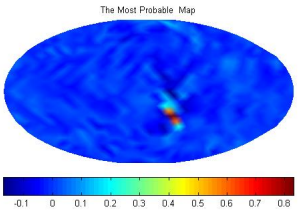

(d) Regularized Reconstruction

Figure 5.8: A Very Strong Point Source : When the source is strong, there is no need of regularization. It is clear from the panel (c) and (d) that regularization brings no significant improvemnet in reconstruction. A regularization strength $\lambda = 3$ is used. Increasing λ to a large value smears out the image and is unfavorable.

5.6 Bias Introduced by Regularization

The map reconstructed map using regularization is a biased estimator while the unregularized reconstruction is unbiased. Regularization introduce the bias in the reconstructed map and alters the pixel-to-pixel co-variance matrix of the reconstructed map. For unregularized reconstruction,

$$< \hat{S} >= (B^T N^{-1} B)^{-1} B^T N^{-1} B S_{true} = S_{true} \tag{5.27}$$

Bias $\mathcal{B}$ is defined as the difference between the S_{true} and $< \hat{S} >$. It is clear that $\mathcal{B} = 0$ for unregularized deconvolution. For the case of regularized deconvolution,

$$\hat{S} = (B^T N^{-1} B + \lambda C)^{-1} B^T N^{-1} D \tag{5.28}$$

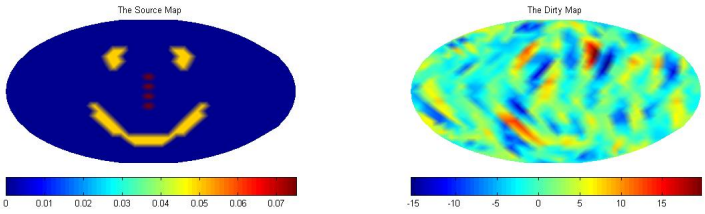

(a) Source Map (b) Dirty Map

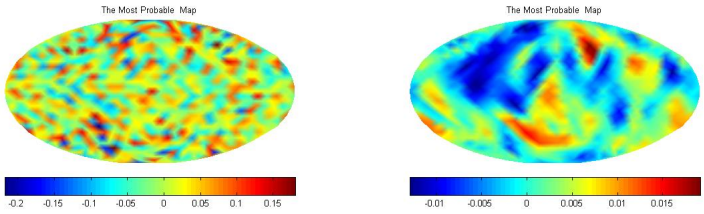

(c) Reconstruction without Regularization (d) Regularized Reconstruction

Figure 5.9: Very Weak Diffused Source : When the source is very weak, a blind regularization like gradient regularization does not help much. Although, there is an improvement, from the panel (c) and (d) it is clear that reconstruction is unreliable.

And,

$$< \hat{S} > = < (B^T N^{-1} B + \lambda C)^{-1} B^T N^{-1} D > \quad (5.29)$$

$$= (B^T N^{-1} B + \lambda C)^{-1} B^T N^{-1} < B S_{true} + n > \quad (5.30)$$

$$= (B^T N^{-1} B + \lambda C)^{-1} B^T N^{-1} B S_{true} \quad (5.31)$$

When N=B the above expression reduces to,

$$< \hat{S} >= (B + \lambda C)^{-1} B S_{true} \quad (5.32)$$

The bias $\mathcal{B}$ for this case is,

$$\mathcal{B} = S_{true} - < \hat{S} >= (1 - (B + \lambda C)^{-1} B) S_{true} \quad (5.33)$$

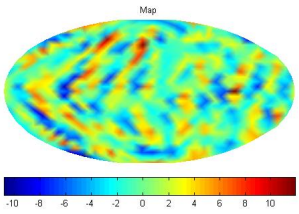

(a) Noise-Only Dirty Map

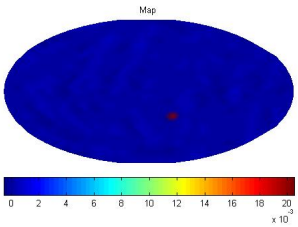

(b) Prior Map

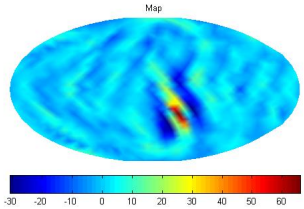

(c) Regularized Reconstruction

Figure 5.10: Noise Only Map : When regularization function in Eq. 5.23 is used, we find that the prior introduces a bias sufficient to obtain signal even from pure noise map. This is dangerous as it leads to spurious detection

5.7 Discussion

The above results demonstrate the merits of incorporating gradient regularization. Figures 5.5, 5.6 and 5.7 clearly show that gradient regularized reconstruction brings a significant visual improvement. Here, the difference in intensities of two neighboring pixels is penalized. There is a preference towards reconstructed map that has less random fluctuations leading to a noise suppression effect. For a qualitative measure of the improvement, one can compare the NSP value of the regularized and the unregularized reconstruction. The NSP_{reg} is significantly higher than NSP_{unreg} for weak sources (refer row 1,2 and 3 of the table).

At this point, it is worth highlighting that gradient regularization is a blind prior. It contains no information about the location of the source. Therefore, the bias introduced by implementing gradient regularization does not pose a threat of false detection. The only disadvantage in using smoothness of the reconstructed map as a prior is that information about the small scale

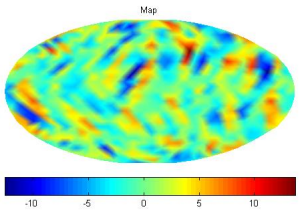

(a) Noise-Only Dirty Map

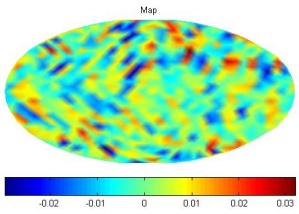

(b) Clean Map for Noise Only Case

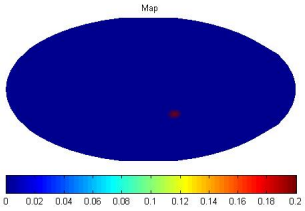

(c) Prior Map

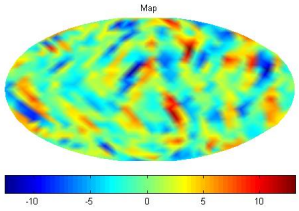

(d) Dirty Map with Faint Source

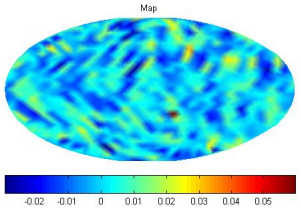

(e) Reconstruction for Faint Source Using the Source Location as Prior in Regularization

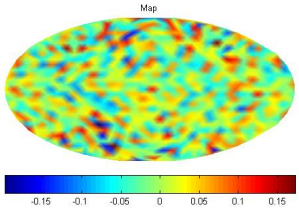

(f) Reconstruction for Faint Source Using Norm Regularization

Figure 5.11: Source reconstruction using Prior Knowledge on Source Location : We use the modified norm regularization function that incorporates the source location information. We find that signal is picked up only in presence of signal. One can compare the results obtained on incorporating prior knowlwdge of the source again results obtained using norm (blind) regularization.

structure might get wiped off when strength of regularization is high. For instance, if we over-regularize deconvolution of a very strong diffused source, its blurs out and the details in its structure is lost.

Further, we find that the optimal choice for regularization strength depends on the data itself. More the map is contaminated with noise, more is the necessity to implement prior information and higher should be the value of λ. As we increase λ, the value of $\chi^2(S)$ increases and value of penalty function $R(S)$ decreases. For instance, for very high value of λ, the small-scale structures in the reconstructed map is completely removed. For very low value of λ, over-fitting of the data takes place. The strength of regularization dictates the weight on these two competing functions. In our analysis, we set the strength for regularization (λ) by numerically solving Eq. 5.16.

In Figure 5.8, we investigate the effect of regularization in an extreme case. Here the source injected is very bright. In such cases, one expects that regularization should not bring significant difference to the reconstruction. From this figure, one can see that regularization is, indeed, unnecessary when the source is bright. The improvement in the value of NSP of the regularized map is very tiny compared to NSP of unregularized map (refer row 4 of the table). The source map contains sufficient uncontaminated information and adding a prior doesn't really improve the recovery.

Figure 5.9 considers the other extreme scenario where the injected source is very faint. The dirty map is highly contaminated with noise and a blind prior like gradient regularization is not sufficient to produce a faithful reconstruction. However, if we happen to know some information on the source location, incorporating this information appropriately will help to greatly in improving the quality of reconstruction. This is demonstrated in the Figure 5.11.

We implement the prior information on the source location as described in section 5.5. Although this method gives excellent reconstruction even when the signal is very weak, one has to be careful in its implementation. Unlike gradient regularization, the prior in this cases has an explicit information on the source location. There is a preference towards those reconstructed map that have high intensity at that particular location in sky. Over-regularizing thus, will lead to false source reconstruction. Here, it becomes crucial to set a right balance between the weights to the prior information and to the information contained in data. Also, one has to notice that there are two parameters (μ and κ) to be tuned in the regularization function in Eq. 5.24. At the moment, we have set $\mu = 2$ and $\kappa = 10^{-2}$ by trial-and-error method. We have checked that this works well for a wide range of source intensity distribution. Further, it has to be noted that for this choice of μ and κ, the signal is only picked up from the dirty map that has a weak signal and

not from the pure noise map. However, we do not claim that this choice is optimal. In-fact, our future plans include devising an more logical method to chose the value of these factors. We anticipate that for an optimal choice of μ and κ, the quality of reconstructed map can be improved even more. At this point, our only claim is that this form of regularization function has a potential to efficiently reconstruction the true sky even in presence of very weak signals.

Next, we discuss a few differences between regularized deconvolution and the well established likelihood statistic ([Talukder et al., 2011]). In the detection problem, one is interested to know the presence or absence of a particular known pattern in the data. In such a case, likelihood ratio is the optimal detection statistics according to Neyman-Pearson criteria. The assumption here is that the pattern in the sky is accurately known. However, most often in the real scenarios, we only have a partial information about the source intensity distribution and it becomes important to be able to regulate the strength of the prior. Implementing regularization in a Bayesian framework provides this flexibility. Further, even when the source location is completely unknown, it allows us to use blind prior like gradient and norm regularization. At this point one has to also notice that map-making problem is fundamentally different from the detection problem as they address two different questions. Unlike the detection problem where one is interested to know if a particular pattern in present in data, the map-making problem concerns with reconstructing the most probable pattern in the sky given the data. One can then use this reconstructed map to detect the presence or absence of a particular signal.

In the extreme case, where we known the exact source intensity distribution, the problem of map-making becomes similar to the detection problem. It will be interesting to compare the results obtained using our method to the results of maximum likelihood method for this particular case. The primary difference between the two will be that while maximum likelihood ratio is an estimator that is defined on dirty map, the statistic developed using Bayesian inference will be defined on the reconstructed map.

This part of the thesis is still an ongoing work. Our further plan is to use the above result to address the following question - "Given that a stochastic gravitational wave source is located at a particular position in the sky, what can we say about the source parameters in the absence of its detection." Such priors on source location is not unrealistic. For instance, one expects to observe stochastic gravitational waves from the Virgo cluster and its location

is well known to us through the electromagnetic observation. We can use such an analysis to place an upper limit on the parameters of the sources in the Virgo cluster in the absence of its detection.

References

J. Abadie, B. P. Abbott, R. Abbott, M. Abernathy, T. Accadia, F. Acernese, C. Adams, R. Adhikari, P. Ajith, B. Allen, and et al. TOPICAL REVIEW: Predictions for the rates of compact binary coalescences observable by ground-based gravitational-wave detectors. *Classical and Quantum Gravity*, 27(17):173001, September 2010. doi: 10.1088/0264-9381/27/17/173001.

B. P. Abbott, R. Abbott, R. Adhikari, P. Ajith, B. Allen, G. Allen, R. S. Amin, S. B. Anderson, W. G. Anderson, M. A. Arain, and et al. LIGO: the Laser Interferometer Gravitational-Wave Observatory. *Reports on Progress in Physics*, 72(7):076901, July 2009. doi: 10.1088/0034-4885/72/7/076901.

B. Allen and A. C. Ottewill. Detection of anisotropies in the gravitational-wave stochastic background. *Phys. Rev. D*, 56:545–563, July 1997.

B. Allen and J. D. Romano. Detecting a stochastic background of gravitational radiation: Signal processing strategies and sensitivities. *Phys. Rev. D*, 59(10):102001, May 1999. doi: 10.1103/PhysRevD.59.102001.

B. Allen, W. G. Anderson, P. R. Brady, D. A. Brown, and J. D. E. Creighton. FINDCHIRP: An algorithm for detection of gravitational waves from inspiraling compact binaries. *Phys. Rev. D*, 85(12):122006, June 2012. doi: 10.1103/PhysRevD.85.122006.

K. G. Arun and A. Pai. Tests of General Relativity and Alternative Theories of Gravity Using Gravitational Wave Observations. *International Journal of Modern Physics D*, 22:1341012, January 2013. doi: 10.1142/S0218271813410125.

S. Babak, R. Biswas, P. R. Brady, D. A. Brown, K. Cannon, C. D. Capano, J. H. Clayton, T. Cokelaer, J. D. E. Creighton, T. Dent, A. Dietz, S. Fairhurst, N. Fotopoulos, G. González, C. Hanna, I. W. Harry, G. Jones,

D. Keppel, D. J. A. McKechan, L. Pekowsky, S. Privitera, C. Robinson, A. C. Rodriguez, B. S. Sathyaprakash, A. S. Sengupta, M. Vallisneri, R. Vaulin, and A. J. Weinstein. Searching for gravitational waves from binary coalescence. *Phys. Rev. D*, 87(2):024033, January 2013. doi: 10.1103/PhysRevD.87.024033.

R. Balasubramanian and S. V. Dhurandhar. Estimation of parameters of gravitational wave signals from coalescing binaries. *Phys. Rev. D*, 57:3408–3422, March 1998. doi: 10.1103/PhysRevD.57.3408.

L. Blackburn, L. Cadonati, S. Caride, S. Caudill, S. Chatterji, N. Christensen, J. Dalrymple, S. Desai, A. Di Credico, G. Ely, J. Garofoli, L. Goggin, G. González, R. Gouaty, C. Gray, A. Gretarsson, D. Hoak, T. Isogai, E. Katsavounidis, J. Kissel, S. Klimenko, R. A. Mercer, S. Mohapatra, S. Mukherjee, F. Raab, K. Riles, P. Saulson, R. Schofield, P. Shawhan, J. Slutsky, J. R. Smith, R. Stone, C. Vorvick, M. Zanolin, N. Zotov, and J. Zweizig. The LSC glitch group: monitoring noise transients during the fifth LIGO science run. *Classical and Quantum Gravity*, 25(18):184004, September 2008. doi: 10.1088/0264-9381/25/18/184004.

Luc Blanchet, Thibault Damour, Gilles Esposito-Farèse, and Bala R. Iyer. Gravitational radiation from inspiralling compact binaries completed at the third post-newtonian order. *Phys. Rev. Lett.*, 93:091101, Aug 2004. doi: 10.1103/PhysRevLett.93.091101. URL `http://link.aps.org/doi/10.1103/PhysRevLett.93.091101`.

B. J. Brewer and G. F. Lewis. Strong Gravitational Lens Inversion: A Bayesian Approach. *The Astrophysical Journal*, 637:608–619, February 2006. doi: 10.1086/498409.

S. J. Chamberlin and X. Siemens. Stochastic backgrounds in alternative theories of gravity: Overlap reduction functions for pulsar timing arrays. *Phys. Rev. D*, 85(8):082001, April 2012. doi: 10.1103/PhysRevD.85.082001.

E. E. Flanagan. Sensitivity of the Laser Interferometer Gravitational Wave Observatory to a stochastic background, and its dependence on the detector orientations. *Phys. Rev. D*, 48:2389–2407, September 1993. doi: 10.1103/PhysRevD.48.2389.

K. M. Górski, E. Hivon, A. J. Banday, B. D. Wandelt, F. K. Hansen, M. Reinecke, and M. Bartelmann. HEALPix: A Framework for High-Resolution Discretization and Fast Analysis of Data Distributed on the Sphere. *The Astrophyscial Journal* , 622:759–771, April 2005. doi: 10.1086/427976.

Gregory M Harry and the LIGO Scientific Collaboration. Advanced ligo: the next generation of gravitational wave detectors. *Classical and Quantum Gravity*, 27(8):084006, 2010. URL http://stacks.iop.org/0264-9381/27/i=8/a=084006.

J. Hough, S. Rowan, and B. S. Sathyaprakash. The search for gravitational waves. *Journal of Physics B Atomic Molecular Physics*, 38:497, May 2005. doi: 10.1088/0953-4075/38/9/004.

E. Messaritaki and LIGO Scientific Collaboration. Report on the first binary black hole inspiral search in LIGO data. *Classical and Quantum Gravity*, 22:1119, September 2005. doi: 10.1088/0264-9381/22/18/S26.

S. Mitra, S. Dhurandhar, T. Souradeep, A. Lazzarini, V. Mandic, S. Bose, and S. Ballmer. Gravitational wave radiometry: Mapping a stochastic gravitational wave background. *Phys. Rev. D*, 77(4):042002, February 2008.

S. D. Mohanty and S. V. Dhurandhar. Hierarchical search strategy for the detection of gravitational waves from coalescing binaries. *Phys. Rev. D*, 54:7108–7128, Dec 1996. doi: 10.1103/PhysRevD.54.7108. URL http://link.aps.org/doi/10.1103/PhysRevD.54.7108.

Benjamin J. Owen. Search templates for gravitational waves from inspiraling binaries: Choice of template spacing. *Phys. Rev. D*, 53:6749–6761, Jun 1996. doi: 10.1103/PhysRevD.53.6749. URL http://link.aps.org/doi/10.1103/PhysRevD.53.6749.

P. C. Peters and J. Mathews. Gravitational radiation from point masses in a keplerian orbit. *Phys. Rev.*, 131:435–440, Jul 1963. doi: 10.1103/PhysRev.131.435. URL http://link.aps.org/doi/10.1103/PhysRev.131.435.

B. S. Sathyaprakash and S. V. Dhurandhar. Choice of filters for the detection of gravitational waves from coalescing binaries. *Phys. Rev. D*, 44:3819–3834, Dec 1991. doi: 10.1103/PhysRevD.44.3819. URL http://link.aps.org/doi/10.1103/PhysRevD.44.3819.

B.S. Sathyaprakash and Bernard F. Schutz. Physics, astrophysics and cosmology with gravitational waves. *Living Reviews in Relativity*, 12(2), 2009. URL http://www.livingreviews.org/lrr-2009-2.

A. S. Sengupta, S. V. Dhurandhar, A. Lazzarini, and T. Prince. Extended hierarchical search (EHS) algorithm for detection of gravitational waves

from inspiralling compact binaries. *Classical and Quantum Gravity*, 19: 1507–1512, April 2002. doi: 10.1088/0264-9381/19/7/337.

S. H. Suyu, P. J. Marshall, M. P. Hobson, and R. D. Blandford. A Bayesian analysis of regularized source inversions in gravitational lensing. *Monthly Notices of the Royal Astronomical Society*, 371:983–998, September 2006. doi: 10.1111/j.1365-2966.2006.10733.x.

Dipongkar Talukder, Sanjit Mitra, and Sukanta Bose. Multibaseline gravitational wave radiometry. *Phys. Rev. D*, 83:063002, Mar 2011. doi: 10.1103/PhysRevD.83.063002. URL `http://link.aps.org/doi/10.1103/PhysRevD.83.063002`.

K. S. Thorne. Gravitational Radiation – A New Window Onto the Universe. *ArXiv General Relativity and Quantum Cosmology e-prints*, April 1997.

M. Vallisneri. Testing general relativity with gravitational waves: A reality check. *Phys. Rev. D*, 86(8):082001, October 2012. doi: 10.1103/PhysRevD.86.082001.

S. J. Warren and S. Dye. Semilinear Gravitational Lens Inversion. *The Astrophysical Journal*, 590:673–682, June 2003. doi: 10.1086/375132.

J. M. Weisberg and J. H. Taylor. Relativistic Binary Pulsar B1913+16: Thirty Years of Observations and Analysis. *ArXiv Astrophysics e-prints*, July 2004.

Appendix A

Stationary Phase Approximation

In this section we shall briefly discuss the stationary phase approximation. Physically, this approximation uses the fact that a rapidly oscillating phase intergrated over a long duration cancels itself. The contribution to the integral dominantly comes from stationary point of phase. It is a very useful tool that has been used many times in the work described below to evaluate the integral of the following form -

$$I = \int_{-\infty}^{\infty} F(x) e^{-i\phi(x)}\, dx\,. \tag{A.1}$$

If x_s is the stationary point of the phase, such that

$$\phi'(x_s) = 0 \tag{A.2}$$

We can expand the phase about the stationary point as -

$$\phi(x) \approx \phi(x_s) + \frac{1}{2}\phi''(x_s)(x - x_s)^2 \tag{A.3}$$

The integral becomes ,

$$I \approx F(x_s) e^{-i\phi(x_s)} \int_{-\infty}^{\infty} e^{-i\phi(x_s)\frac{(x-x_s)^2}{2}}\, dx\,. \tag{A.4}$$

Finally, from this one can obtain,

$$I \approx \sqrt{\frac{2\pi}{i\phi''(x_s)}} F(x_s) e^{-i\phi(x_s)} \tag{A.5}$$

Appendix B

Derivation of expression for S_{ml}

The most likely solution S_{ml} is got by minimizing the χ^2 value with respect to S.

$$\frac{1}{2}\chi^2 = \frac{1}{2}(BS - D)^T N^{-1}(BS - D) \tag{B.1}$$

Minimizing,

$$\nabla_s(\chi^2) = \frac{D}{dS}((BS - D)^T N^{-1}(BS - D)) \tag{B.2}$$

Using the product rule of differentiation,

$$\nabla_s(\chi^2) = (\frac{d}{dS}(BS-D))^T N^{-1}(BS-D)+(BS-D)^T N^{-1}\frac{d}{dS}(BS-D) \tag{B.3}$$

Using the result, $\frac{d}{dx}Ax = A^T$ and the using the fact that B is symmetric we get,

$$\nabla_s(\chi^2) = BN^{-1}(BS - D) + (BS - D)^T N^{-1}B = 2B^T N^{-1}(BS - D) \tag{B.4}$$

This quantity should be equal to zero for $S = S_{ml}$. So, to find S_{ml}, we set the above expression to zero

$$B^T N^{-1}(BS - D) = 0 \tag{B.5}$$

On rearranging the equation we get,

$$S_{ml} = (B^T N^{-1} B)^{-1} B^T N^{-1} D \tag{B.6}$$

But the pixel-to-pixel covariance matrix N is proportional to beam matrix B. Using this, we can simplify the above equation further as,

$$S_{ml} = B^{-1} D \tag{B.7}$$

Appendix C

Derivation of expression for S_{mp}

The most probable solution is got by maximizing the posterior probability, which is equivalent to minimizing the value of M(S).

$$M(S) = \chi^2 + \lambda R(S)^2 \tag{C.1}$$

If the source covariance matrix is denoted by $Q =< SS^T >$, then by analogy

$$\lambda R(S) = S^T Q^{-1} S \tag{C.2}$$

On comparing with the taylor expansion of $R(S)$ about $S_{reg} = 0$, it can be identified that,

$$Q = (\lambda C)^{-1} \tag{C.3}$$

Using the above arguments, it is clear that M(S) can be expressed as,

$$M(S) == (BS - D)^T N^{-1} (BS - D) + S^T (Q)^{-1} S \tag{C.4}$$

$\nabla M(S) = 0$ for $S = S_{ml}$. So we find S_{ml}S by setting the expression to zero

$$B^T N^{-1} (BS - D) + Q^{-1} = 0 \tag{C.5}$$

On simplification we get,

$$S_{mp} = (S^{-1} + B^T N^{-1} B)^{-1} B^T N^{-1} D \tag{C.6}$$

Now, if we define A to be the hessian matrix of M(S)

$$A = \nabla\nabla M(S) = B + \lambda C \tag{C.7}$$

Further, we write the explicit form of A by double differentiating A with respect to S

$$A = Q^{-1} + B^T N^{-1} B = Q^{-1} + \nabla\nabla\chi^2 \tag{C.8}$$

Rearranging S_{mp} to express in terms of A and $\nabla\nabla\chi^2$,

$$S_{mp} = (Q^{-1} + B^T N^{-1} B)^{-1} B^T N^{-1} D = A^{-1} B^T N^{-1} D \tag{C.9}$$

$$= A^{-1}(\nabla\nabla\chi^2)(\nabla\nabla\chi^2)^{-1} B^T N^{-1} D = A^{-1}(\nabla\nabla\chi^2) S_{ml} \tag{C.10}$$

This further simplifies to

$$S_{mp} = (B + \lambda C)^{-1} D \tag{C.11}$$